Cohesive Zone Failure Modelling of Polymeric Adhesives used in Ceramic/Metal Armor

Harshil Pisavadia[a], Geneviève Toussaint[b], Patricia Dolez[c], James D. Hogan[a]

[a]*Department of Mechanical Engineering, University of Alberta, Edmonton, AB T6G 2R3, Canada*
[b]*Defence Research and Development Canada, Valcartier Research Center, Quebec City, QC G3J 1X5, Canada*
[c]*Department of Human Ecology, University of Alberta, Edmonton, AB T6G 2R3, Canada*

Abstract

In this paper, a trilinear cohesive zone modelling approach available in the explicit non-linear finite element software LS-DYNA is used to model the dynamic impact failure of an adhesive layer. This approach is an improvement over simpler cohesive zone models presented in the literature. The model is validated for the SikaForce^{TM6} 7752-L60 polyurethane adhesive using force-displacement curves of double cantilever beam and end-notched flexure tests extracted from the literature. The trilinear cohesive zone model was then implemented to simulate the behavior of the adhesive bonding a ceramic alumina tile to an aluminium backing. Simulations were performed to explore the effect of the adhesive layer thickness, manufacturing defects (air bubbles simulated through deleted elements), and strain rates. It was found that: (1) a thicker adhesive layer decreased the ceramic/metal armor performance for a single hit, but resulted in a reduction of the damage area of the top ceramic tile in simulations; (2) an increase in the amount of defects resulted in greater depth of penetration and increased delays to stop the projectile, resulting in a reduction of simulated armor performance; and (3) including strain rate effects in the model resulted in predictions of a reduced depth of penetration and an increase in the damage region of the interlayer after the impact event for all of the simulated impact velocities, thereby predicting a decreased performance for multi-hit impact conditions of the armor system.

Keywords: Ceramic/metal, armor system, cohesive zone modelling, ballistic impact, adhesive failure, adhesive defects

Nomenclature

General material properties

ν Poisson's ratio

ρ Density

E Young's modulus

G Shear modulus

S Shear strength

T Yield strength

Geometrical and load symbols

δ Separation displacement

a_0 Initial crack length

L_{DCB} Beam length

L_{ENF} Midspan length

P Applied load

p Pressure

t_A Adhesive thickness

t_P Adherend thickness

Subscripts

S Shear stress

T Tensile stress

Cohesive zone model parameters

$\dot{\varepsilon}_S$ Equivalent strain rate term of shear stress

$\dot{\varepsilon}_T$ Equivalent strain rate term of yield stress

$\dot{\varepsilon}_{Gi}$ Equivalent strain rate term of mode i critical energy release rate (i=I,II)

γ_i Mode i critical energy release rate coefficient (i=I,II)

τ_i Mode i critical energy release rate exponent (i=I,II)

f_{Gi} Mode i plastic to total area ratio (i=I,II)

G_{iC} Mode i critical energy release rate (i=I,II)

G_{ij} Lower (j=0) and upper (j=∞) bound of mode i critical energy release rate (i=I,II)

S_j Lower bound (j=0) and upper bound (j=1) of shear stress

T_j Lower bound (j=0) and upper bound (j=1) of yield stress

Johnson-Holmquist II model parameters

β Bulking constant

$\dot{\varepsilon}_{\mathrm{JH2}}$ Johnson-Holmquist II reference strain rate

μ_{JH2} Johnson-Holmquist II excess compression term

a_{JH2} Johnson-Holmquist II intact strength constant

b_{JH2} Johnson-Holmquist II fractured strength constant

c_{JH2} Johnson-Holmquist II strain rate constant

d_1 Damage constant

d_2 Damage exponent

FS Failure strain

HEL Hugoniot elastic limit

k_i Bulk modulus (i=1); ith pressure coefficient (i=2,3)

m_{JH2} Johnson-Holmquist II fractured strength exponent

n_{JH2} Johnson-Holmquist II intact strength component

p^* Maximum tensile strength

p_{HEL} Pressure at HEL

SF_{MAX} Maximum fracture strength ratio

Johnson-Cook model parameters

$\dot{\varepsilon}_{\mathrm{JC}}$ Johnson-Cook reference strain rate

μ_{JC} Johnson-Cook excess compression term

b_{JC} Johnson-Cook hardening constant

C_1 Bulk modulus for the linear equation of state

c_{JC} Johnson-Cook strain rate constant

C_P Specific heat

D_i Failure parameter i (i=1,2,3,4,5)

m_{JC} Johnson-Cook thermal softening exponent

n_{JC} Johnson-Cook hardening exponent

T_{melt} Melting temperature

T_{room} Room temperature

Mie-Gruneisen model parameters

γ_0 Gruneisen gamma

a First order volume correction to Gruneisen gamma

C Intercept to the cubic shock-velocity versus particle velocity curve

$S_{\text{MG},i}$ Coefficient i to the cubic shock-velocity versus particle velocity curve (i=1,2,3)

Abbreviations

2D Two-dimensional

3D Three-dimensional

CZM Cohesive zone model

DCB Double cantilever beam

DOP Depth of penetration

ENF End-notched flexure

JC Johnson-Cook

JH2 Johnson-Holmquist II

TAST Thick adherend shear test

TCZM Trilinear cohesive zone model

TSL Traction separation law

$P-\delta$ Load-displacement

1. Introduction

1.1 Ceramic/metal armor

The performance of armor systems can be improved by better designing the adhesive layer used to bond the ceramic tiles to the metal backing layer in the armor system [1]. Here, the adhesive layer plays a critical role during impact in controlling wave propagation that leads to damage accumulation within the armor structure, ultimately affecting armor performance [2]. In the open literature, some experimental and numerical studies have investigated the effects adhesives have on the performance of armor systems. For example, Zaera et al. [3] explored the effects that different thicknesses (0.5 mm to 1.5 mm) of polyurethane and epoxy resin adhesives have on armor efficiency. It was concluded that thicker adhesives caused more damage to the ceramic tile, and this damage was due to the ceramic being unsupported by the backing for a greater period of time; however, a thicker layer of adhesives reduced the degree of fragmentation of the adjacent tiles. In another study, López-Puente et al. [4] identified three different factors related to the adhesive thickness performance that have an influence on the armor efficiency: shear stress, ceramic spalling, and energy absorption. They concluded that an epoxy adhesive thickness of 0.3 mm was optimum to (1) minimize adhesive shear stress, (2) minimize ceramic spalling, and (3) increase the energy absorption mechanism of the metal backing for armors consisting of an alumina ceramic plate bonded to an aluminum metal backing. In a separate study, Shen et al. [5] performed experimental and numerical studies to investigate the effect of the adhesive layer thicknesses (0.2 mm to 3.0 mm) on the ceramic/metal armor. It was concluded that the optimum adhesive layer during multi-hit impact conditions was 2 mm. In their studies, Prakash et al. [6] and Arslan et al. [7] performed numerical simulations using a Cowper-Symonds strength model and an elastic-plastic material model to model their epoxy adhesive layer within an armor system. Prakash et al. [6] found that a thicker adhesive also led to greater plastic deformation in the metal backing layer, and Arslan et al. [7] concluded that the residual velocity of the projectile was found to increase with increasing adhesive thickness. Therefore, both of these studies found that increasing the adhesive thicknesses decreases the armor performance. In a separate study, Seifert et al. [8] performed experimental tests to investigate the effects of the adhesive stiffness on the armor performance and they found that a higher fracture strain led to greater deformation in the backing plate and adhesion strength was found to be dependent on loading rates. Overall, studies have shown that a thin adhesive layer has better performance against a single shot, however, during multi-hit impact conditions, a thicker adhesive layer reduce the degree of fragmentation and damage to adjacent tiles. Further, when studying the effect of adhesive thickness on the overall armor performance, the above numerical studies did not take into consideration the functional relationships between the adhesive material and its geometrical properties [9, 10], as we do in the current study.

1.2 Adhesive models

The cohesive zone modelling (CZM) approach is a widely used technique to model adhesive joints [5, 11, 12, 13, 14, 15] and interfaces where interlaminar damage (e.g., delamination) occurs [16, 17, 18]. However, limited studies have utilized this energy-based approach to numerically characterize strength and fracture of adhesives used in armor applications [5, 11, 19]. In these examples, the bilinear CZM approach was used by Bürger et al. [11] and Goda and Girardot [19] to model the adhesive layer of ceramic/fiber

reinforced composite armors and by Shen et al. [5] to model the adhesive layer bonding ceramics to a metal backing. These studies did not consider plasticity in the adhesive material as they used the bilinear approach for the traction separation law. Therefore, we improve upon this in the current study by considering plastic behavior during separation at failure through the trilinear (or trapezoidal) traction separation law. Using this new formulation, the dynamic failure of adhesives is more accurately predicted [20]. To date, no studies have considered using the trilinear cohesive zone model (TCZM) to represent the adhesive layer bonding the ceramic tiles to a metal backing layer. In another study, Jia et al. [21] studied the effects that high strain rates have on polyurethane adhesives with validations using the thick adherend shear test (TAST), the double cantilever beam (DCB) test, and the end-notched flexure (ENF) test. It was concluded that the adhesive can be simulated using a strain rate-dependent CZM approach under various impact conditions, and this will be the approach taken in this paper. Building on these, this present investigation expands the research of previous studies by considering functional dependency of crucial adhesive material properties (i.e., modes I and II critical energy release rates) due to changes in thickness while using a trapezoidal traction separation law to consider plasticity in the cohesive elements. In addition, no studies have yet considered the effect of realistic manufacturing problems such as trapped air within the adhesive layer in composite armor structures, as we do here. This is an important aspect to consider since the performance of these systems can be heavily affected by challenges in quality control (i.e., manufacturing defects).

Finally, the damage resulting from ballistic impact on composite structures consists of complex failure mechanisms. Specifically, the damage response needs to be accurately simulated within each of the composite layers (including the front ceramic tile, metal backing layer, and the adhesive used to bond the system together) and the projectile, including the interaction between each of these subsystems [19]. Therefore, both interlaminar and intralaminar damage are important to consider to accurately predict damage under loading when modelling interfaces in composite structures [17, 18]. Here, Maziz et al. [17] and Maziz et al. [18] evaluated intralaminar damage (e.g., matrix cracks and fiber failures) of pressurized hybrid pipe structures using the Hashin criteria, and interlaminar damage (e.g., ply delamination) was modelled using the bilinear cohesive law.

Motivated by these past investigations, this study applies a mixed-mode trilinear cohesive zone damage model to simulate impact-induced fractures in polymeric adhesives to be used in ceramic/metallic armor of vehicles. In the current work, the TCZM was implemented in the explicit nonlinear finite element software, LS-DYNA code version R11.1.0 [22]. This new approach improves the modelling of system-scale armor [6, 23] by including damage [24], plasticity [25], and rate-dependent terms [20], and also enables simulating initiation and cracks growth within the adhesive layer [11]. These important considerations lead to improved layers delamination modelling of the layers in the structure which has been shown to be critical in the overall performance of armor systems [5]. The TCZM implementation for the adhesive is validated first by comparing numerical results to mechanical test results obtained for the double cantilever beam and end-notched flexure tests [26], followed by a comparison with ballistic simulation data extracted from the literature [6, 23]. Once validated, simulations are then performed to explore how performance is affected by the adhesive thickness and strain rates. For the first time in the literature, this work attempts to provide a better understanding of: (1) the interplay between the critical energy release rate and change in adhesive thicknesses, (2) the effects of manufacturing defects such as air bubbles trapped within the adhesive

layer (defects in the form of deleted cohesive zone elements) on performance, and (3) the role of strain rate-dependent parameters of the adhesive material on the ballistic response of ceramic/metal armors. These new understandings are achieved through incorporating an elastic-plastic trilinear cohesive zone method that improves upon other studies in the literature [5, 19]. In addition, we also consider more realistic simulation setups: (1) uncertainty from experiments is considered in the cohesive zone model due to variability in both the experimental procedures and materials, (2) depth of penetration is analyzed over the entire impact timeframe to better visualize the times in which the projectile penetrates each of the individual layers of the armor structure, and (3) variabilities of cohesive parameters are considered by varying adhesive thicknesses.

2. Validation

This section discusses the validation of both the adhesive and the ceramic/metal armor models. Experimental data of the SikaForce^{TM6} 7752-L60 polyurethane adhesive from Faneco et al. [26] is used to validate the adhesive model. Numerical data from Prakash et al. [6] and Rashed et al. [23] are used to validate the ballistic response of a projectile impacting a ceramic/metal armor system.

2.1 Cohesive zone adhesive model

The CZM parameters for the SikaForce^{TM6} 7752-L60 polyurethane adhesive are obtained from experimental results provided by Faneco et al. [26]. Tensile and shear mechanical properties are obtained from bulk tensile and thick adherend shear test (TAST) results, respectively. The tensile properties include the Young's modulus, E (Pa), and the yield strength, T (Pa). The shear properties include the shear modulus, G (Pa), and the shear strength, S (Pa). The tensile and shear strain energy release rate parameters, G_{IC} (N/m) and G_{IIC} (N/m), are obtained from the double cantilever beam test (DCB) (mode I) and the end-notched flexure test (ENF) (mode II), respectively. These two parameters are the most important parameters in CZM as they govern the onset of adhesive failure [27]. Details of the TCZM technique used in the simulations are detailed in Appendix A.

The experimental layouts of DCB and ENF tests performed by Faneco et al. [26] are presented in Fig. 1, where the top and bottom bars represent the adherends and the shaded region between the bars represent the adhesive layer. In both Fig. 1a and 1b, P (N) is the applied load, δ (m) is the separation displacement, a_0 (m) is the initial crack length, t_A (m) is the adhesive thickness, and t_P (m) is the adherend thickness. L_{DCB} (m) and L_{ENF} (m) are the beam length and the midspan length for the DCB and ENF test specimens, respectively. More details of the experimental setup of the DCB and ENF tests can be found in the study by Faneco et al. [26]. Aluminum is used as the upper and lower adherends for the DCB and ENF tests based on the setup of Faneco et al. [26]. The SikaForce^{TM6} 7752-L60 polyurethane is used as the representative adhesive layer material in our current models. An adhesive thickness of 1 mm is used for the DCB and ENF tests following Faneco et al. [26]. Note that it is very important to consider the placement of the hinges and applied load when numerically simulating these tests as these influence the stiffness of the entire setup, and so great care is given in these simulations to match the setups from Faneco et al. [26]. A schematic of the numerical model replicating the experimental test setup from Faneco et al. [26] is provided in Appendix B Fig. B.16. Appendix B further details the element formulation and contact definitions used in these simulations.

These model parameters determined from the experiments are summarized in Table 1, where strain rate effects are not included for these quasi-static loading conditions. The density of the adhesive is obtained from the material datasheet provided by the adhesive manufacturer [28]. When conducting these simulations, experimental and material variabilities are accounted for by using the minimum and maximum values of all the mechanical properties to one standard deviation of the mean as measured by Faneco et al. [26].

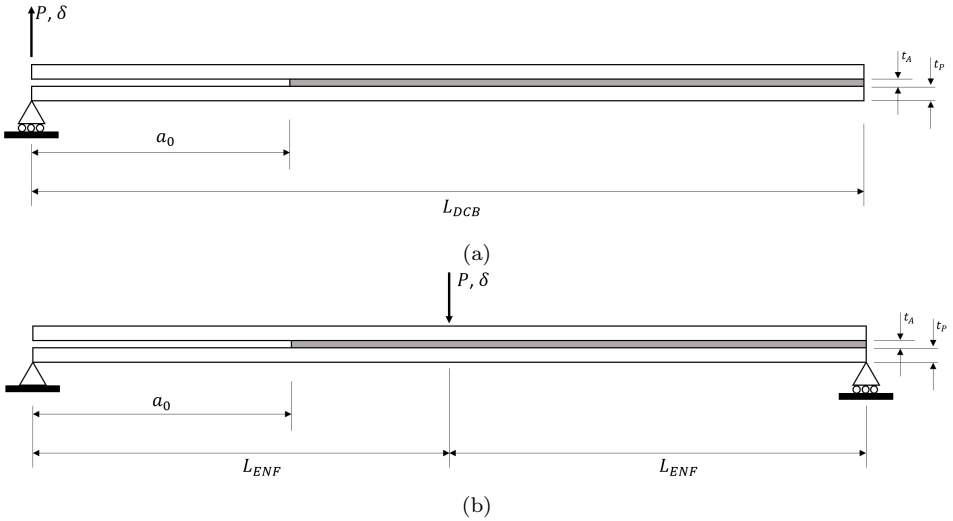

Figure 1: Experimental layout of the (a) double cantilever beam and (b) end-notched flexure tests used to numerically characterize strength and fracture of adhesives. A three-dimensional numerical model is constructed based on this layout (shown in Appendix B).

Table 1: Trilinear cohesive zone model parameters used to define the SikaForce^{TM6} 7752-L60 polyurethane adhesive in LS-DYNA [26, 28, 29].

Model Parameters	Value	Units
Density (ρ) [28]	1600	kg/m^3
Young's modulus (E) [26]	$4.93(\pm0.90)\times10^8$	Pa
Shear modulus (G) [26]	$1.88(\pm0.16)\times10^8$	Pa
Yield strength (T) [26]	$3.24(\pm0.48)\times10^6$	Pa
Shear strength (S) [26]	$5.16(\pm1.14)\times10^6$	Pa
Lower bound of mode I critical energy release rate (G_{I0}) [26]	$2.36(\pm0.17)\times10^3$	N/m
Lower bound of mode II critical energy release rate (G_{II0}) [26]	$5.41(\pm0.47)\times10^3$	N/m
Mode I plastic to total area ratio (f_{G1}) [29]	0.13	-
Mode II plastic to total area ratio (f_{G2}) [29]	0.9	-

A plastic kinematic model (`*MAT_PLASTIC_KINEMATIC`) is implemented for the aluminum (AA6082 T651) adherends. This model is chosen since it considers isotropic and kinematic hardening plasticity behaviors [31]. Material parameters for the aluminum adherend are obtained from Faneco et al. [26] and the Poisson's ratio is obtained from Shengze et al. [30]. These parameters are summarized in Table 2.

Table 2: Plastic kinematic model parameters used to define the aluminum adherends (AA6082 T651) in LS-DYNA [26, 30].

Model Parameters	Value	Units
Density (ρ)	2.79×10^{3}	kg/m^3
Young's modulus (E)	$7.01(\pm0.08)\times10^{10}$	Pa
Poisson's ratio (ν)	0.269	-
Yield strength (T)	$2.62(\pm0.08)\times10^{8}$	Pa

To perform model validation, three-dimensional models of the DCB and ENF tests are set up in LS-DYNA. These DCB and ENF tests have been used to acquire model parameters for adhesives used in many applications and studies [11, 16, 27, 32, 33]. In this current study, model validation includes comparisons between experimentally obtained and simulated load-displacement ($P-\delta$) curves from the DCB and ENF tests, as well as considerations for mesh sensitivity of these results (shown later in Fig. 3).

Comparisons between the experimentally obtained DCB and ENF $P-\delta$ curves from Faneco et al. [26] and simulation results are presented in Fig. 2 using an element size of 1 mm. The simulated data consider the variability in material properties of the adhesive where the upper and lower bounds of the simulated data are obtained from using the maximum and minimum mechanical and fracture properties of the adhesive within one standard deviation as provided by Faneco et al. [26]. The bounded region of the simulated data from Fig. 2 also considers the uncertainty of the hinge placement locations in the experimental setup performed by Faneco et al. [26]. In total, 14 simulations were performed each for the DCB and ENF test configurations. For both the DCB and ENF configurations in Fig. 2, the initial elastic region, peak load, and damage initiation to failure are in reasonable agreement to the experimental data. Specifically, the absolute peak error difference is 1.1% for the DCB test and 5.3% for the ENF test. For all other conditions, both the experimental and simulated curves overlap well, and thus our implementation of the adhesive model is considered validated for simple mechanical testing.

Mesh sensitivity analysis is also performed by generating the $P-\delta$ curves using: (1) coarse: 2 mm; (2) medium: 1 mm; and (3) fine: 0.5 mm element sizes. These sizes are informed by the common element size selection from the literature [15, 32, 34]. The results from the mesh study are presented in Fig. 3 for both the DCB and ENF tests. From Fig. 3, the results show convergence for the 0.5 mm and 1 mm element size for both type of tests.

2.2 Ceramic/metal armor model

A three-dimensional (3D) armor model consisting of 99.5% purity alumina ceramic tile bonded with an epoxy layer to an aluminum Al5083 H116 backing is created to represent the two-dimensional (2D) model given by Prakash et al. [6] and Rashed et al. [23]. The 3D geometry in this investigation is chosen over a 2D geometry as used by Prakash et al. [6] and Rashed et al. [23] since 3D cohesive elements are implemented later in this study. The 3D model in the current investigation simulates a 7.62 mm projectile made of steel 4340 (length of 34 mm and mass of 10.3 g) impacting a ceramic/metal layered structure at 830 m/s. A schematic of this model with its dimensions and the medium-sized mesh is presented in Fig. 4. The number of elements for each of the model constituents is provided in Table 3. The outside cylindrical face of the model is fully

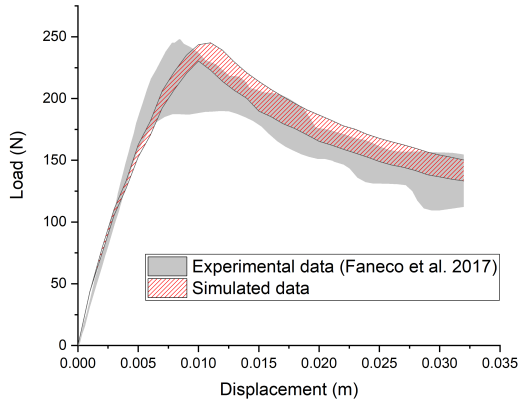

(a)

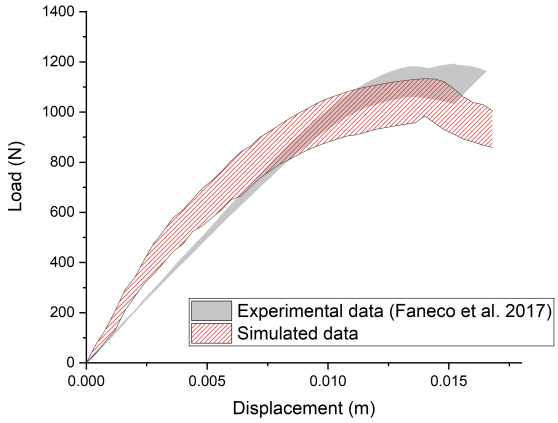

(b)

Figure 2: Comparison between experimentally and numerically obtained load-displacement curves for the (a) double cantilever beam and (b) end-notched flexure tests. Experimental data are obtained from results by Faneco et al. [26].

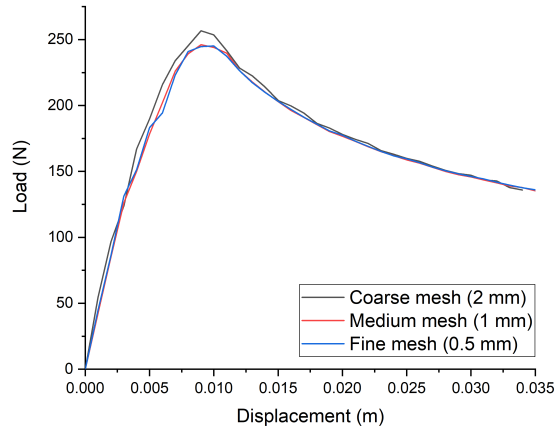

(a)

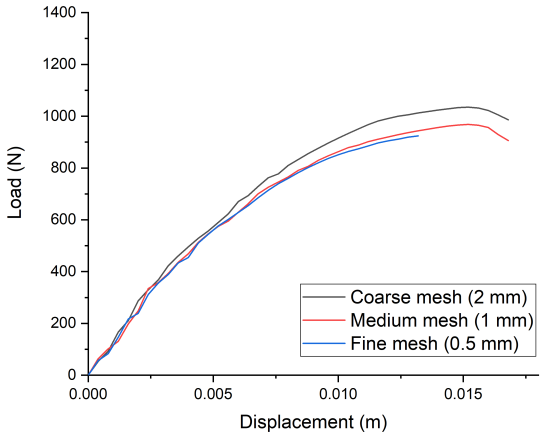

(b)

Figure 3: Load-displacement results from the mesh sensitivity analysis for the (a) double cantilever beam test and (b) end-notched flexure test.

Table 3: Number of elements used for the medium mesh of the ceramic/metal armor model

Part	Number of elements
Projectile	32300
Ceramic front layer	285824
Adhesive interlayer	25984
Metal backing layer	935424

fixed to simulate clamping as was done by Prakash et al. [6] and Rashed et al. [23]. The model was validated by comparing depth of penetration (DOP) and the projectile velocity-time history provided in published papers [6, 23]. Once the model was validated, the epoxy layer was replaced by the SikaForce^{TM6} 7752-L60 polyurethane adhesive layer. These results are presented later in this paper.

2.2.1 *Constitutive models*

The components and constitutive models used to simulate a 4340 steel 7.62 mm projectile impacting a composite armor consisting of 99.5% purity alumina ceramic tile bonded to an aluminum Al5083 H116 metal backing with a SikaForce^{TM6} 7752-L60 [28] polyurethane adhesive layer are provided in Appendix A. The Johnson-Cook (JC) [36] material model is used to model the projectile and metal backing, the Johnson-Holmquist II (JH2) [37] material model is used to model the ceramic tile, and the trilinear cohesive zone modelling (TCZM) technique [20] is used to simulate the adhesive layer.

The JH2 material model parameters for 99.5% alumina are obtained from Cronin et al. [38] and are summarized in Table 4. The JC material model parameters for aluminum and steel are obtained from Rashed et al. [23] and are summarized in Table 5. The yield stress parameter for the aluminum JC model is modified based on the value from Flores-Johnson et al. [39]. This value corresponds to the yield stress of the aluminum AA7075-T651 alloy tuned for a 3D impact simulation. The epoxy material is modelled using a Cowper-Symonds strength model following [6, 23] and neglecting effects of strain rate. Further details of the strength model are provided in Appendix A. The parameters used to define the epoxy material model are obtained from Rashed et al. [23] and are summarized in Table 6.

To discard the highly distorted regions of the system during impact, an erosion criterion for each of the material models is defined independently. This is performed using the erosion material model (`*MAT_ADD_EROSION`) to allow for failure and erosion of the elements and is commonly used to delete the elements [6, 7, 23, 40, 41, 42]. Default values are used except for the maximum effective strain at failure (`EFFEPS`) input. The values for this parameter are obtained from Prakash et al. [6] for each of the materials and are summarized in Table 7. Details of the element formulation and contact definitions used in the simulations are provided in Appendix C.

Continuum elements are used in the present model to enable coupling and interaction between interlaminar and intralaminar damage [17]. Specifically, damage initiation in the cohesive elements (i.e., interlaminar damage) begins from damage of the front ceramic layer (i.e., intralaminar damage) after impact. As the projectile penetrates, further fragmentation in the ceramic tile occurs, and the metal backing starts to deform which causes the delamination of layers. The interaction of the different damage states in composite structures under impact has been reported in the literature [5]. Specifically, Shen et al.

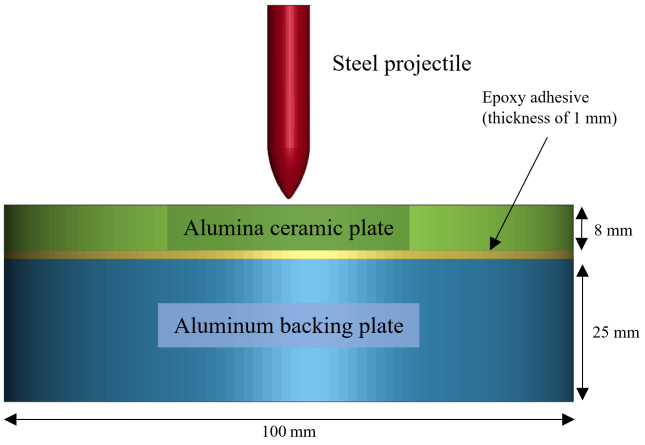

(a)

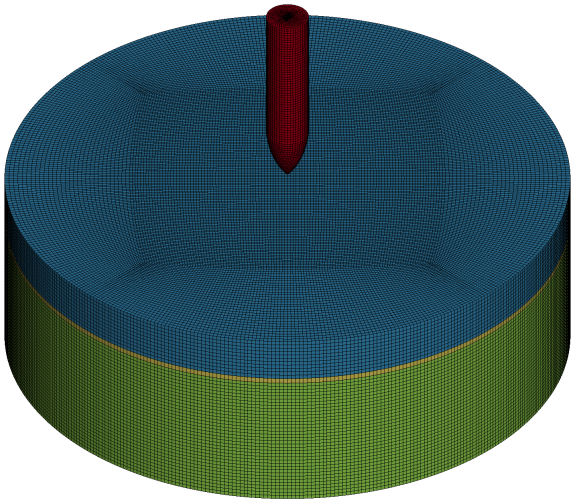

(b)

Figure 4: (a) Front view showing the dimensioned geometry of the 3D layered structure and projectile model and (b) a medium-sized mesh (0.7 mm element size) of the layered structure generated using HyperMesh [35].

Table 4: Johnson-Holmquist II parameters used to define the alumina ceramic tiles in LS-DYNA [38].

Model Parameters	Value	Units
Density (ρ_{JH2})	3700	kg/m^3
Shear modulus (G_{JH2})	90.16×10^9	Pa
Intact strength constant (a_{JH2})	0.93	-
Fractured strength constant (b_{JH2})	0.31	-
Strain rate constant (c_{JH2})	0	1/s
Fractured strength exponent (m_{JH2})	0.6	-
Intact strength component (n_{JH2})	0.6	-
Reference strain rate ($\dot{\varepsilon}_{\mathrm{JH2},0}$)	1	1/s
Maximum tensile strength (p^*)	0.2×10^9	Pa
Maximum fracture strength ratio (SF_{MAX})	0	-
Hugoniot elastic limit (HEL)	2.79×10^9	Pa
Pressure at HEL (p_{HEL})	1.46×10^9	Pa
Bulking constant (β)	1	-
Damage constant (d_1)	0.005	-
Damage exponent (d_2)	1	-
Bulk modulus (k_1)	130.95×10^9	Pa
Second pressure coefficient (k_2)	0	Pa
Third pressure coefficient (k_3)	0	Pa
Failure strain (FS)	1	-

Table 5: Johnson-Cook parameters used to define the aluminum Al5083 H116 metal backing and steel 4340 projectile in LS-DYNA [23, 39].

Model Parameters	Value (Aluminum)	Value (Steel)	Units
Density (ρ_{JC})	2700	7860	kg/m^3
Shear modulus (G_{JC})	26.9×10^9	81.8×10^9	Pa
Yield stress (a_{JC})	0.520×10^9 [39]	0.792×10^9	Pa
Hardening constant (b_{JC})	0.596×10^9	0.510×10^9	Pa
Hardening exponent (n_{JC})	0.551	0.26	-
Strain rate constant (c_{JC})	0.001	0.014	-
Thermal softening exponent (m_{JC})	0.859	1.03	-
Melting temperature (T_{melt})	893	1790	K
Room temperature (T_{room})	300	300	K
Reference strain rate ($\dot{\varepsilon}_{\mathrm{JC},0}$)	1	1	1/s
Specific heat (C_P)	910	477	J/(kg.K)
Failure parameter 1 (D_1)	0.0261	0.05	-
Failure parameter 2 (D_2)	0.263	3.44	-
Failure parameter 3 (D_3)	-0.349	-2.12	-
Failure parameter 4 (D_4)	0.247	0.002	-
Failure parameter 5 (D_5)	16.8	0.61	-
Bulk modulus for the linear EOS (C_1)	58.3×10^9	159×10^9	Pa

Table 6: Mie-Gruneisen model equation of state parameters used to define the epoxy interlayer in LS-DYNA [23].

Model Parameters	Value	Units
Density (ρ)	1186	kg/m^3
Intercept of the $v_s(v_p)$ curve (C)	2730	m/s
Unitless coefficient 1 slope of $v_s(v_p)$ curve ($S_{\mathrm{MG},1}$)	1.493	-
Gruneisen gamma (γ_0)	1.13	-

Table 7: Maximum effective strain at failure values for the erosion material model in LS-DYNA [6, 23]

Material	Maximum effective strain at failure
Alumina [6, 23]	2.0
Aluminum [6, 23]	2.0
Steel [6, 23]	2.1
Epoxy [6, 23]	1.5

[5] reported the adhesive bonding performance (i.e., failure displacement) decreases with increasing adhesive thickness, thus having a negative effect on the overall ballistic performance of the ceramic layer. López-Puente et al. [4] also reported that there was an optimum adhesive layer thickness to get the best performance of the armor system.

Finally, a common element size range used for impact problems of a similar length scale is 0.1 mm to 1 mm [7, 17, 18, 23, 43, 44, 45]. In the current simulations, a coarse, medium, and fine mesh are generated using element sizes of 1 mm, 0.7 mm, and 0.5 mm, respectively. These meshes are generated using the finite element pre-processor, HyperMesh [35].

2.2.2 *Validating the ceramic/metal armor model*

In this sub-section, the ceramic/metal armor model mesh will be validated with numerical results from Prakash et al. [6] and Rashed et al. [23]. The validation cases include a comparison of the velocity-time plot of the projectile and the DOP results. These criteria are chosen since they reasonably evaluate the performance of the armor system [23, 46].

At first, a mesh sensitivity analysis of the ceramic/metal armor model is conducted. Fig. 5 shows the velocity-time history plot of the rear center node of the projectile as it penetrates the layered structure. The rear node is selected for the time history as this was also done in the studies by both Prakash et al. [6] and Rashed et al. [23]. The results obtained are independent of the element size. Therefore, the medium mesh (0.7 mm) is selected for comparison. Fig. 6 shows that the velocity-time history plot of the rear center node of the projectile agrees well with the results provided by Prakash et al. [6] and Rashed et al. [23]. The next step is to validate the DOP results.

The second validation case compares the DOP results obtained with the coarse (1 mm), medium (0.7 mm), and fine (0.5 mm) mesh sizes. The DOP values for each mesh size are obtained by averaging over 6 nodes taken around the central axis at the deepest location of the hole left by the impactor. The DOP results are presented in Table 8. An absolute percentage error difference is calculated in relation to the simulation results of Prakash et al. [6]. Altogether, Fig. 5 and 6, and Table 8 demonstrate that the three-

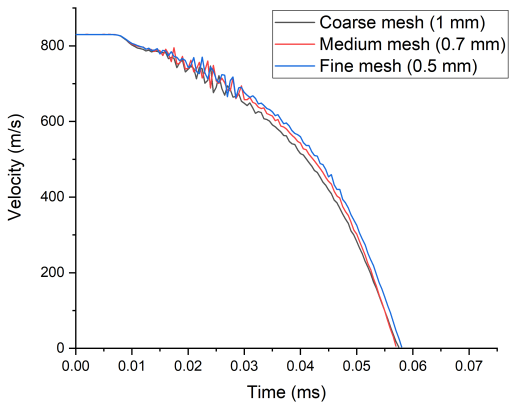

Figure 5: Results from the mesh sensitivity analysis using the velocity-time history of the rear center node of the projectile for the coarse (1 mm), medium (0.7 mm), and fine (0.5 mm) mesh sizes.

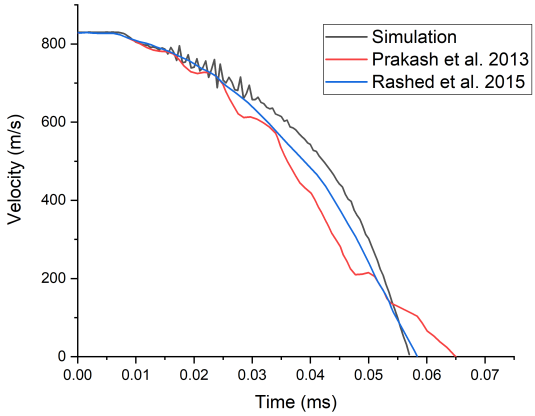

Figure 6: Velocity-time history of the rear center node of the projectile as it penetrates through the armor structure (using the medium mesh). Comparison is made with simulation results by Prakash et al. [6] and Rashed et al. [23].

Table 8: Depth of penetration results using coarse, medium, and fine element sizes. The absolute error difference is calculated relative to the results by Prakash et al. [6].

Mesh	Depth of penetration (mm)	Absolute error difference (%)
Coarse (1 mm)	12.8	8.6
Medium (0.7 mm)	13.9	0.8
Fine (0.5 mm)	14.1	0.6

dimensional impact model is implemented and validated reasonably with published data from the literature. In the next section, the epoxy adhesive that is initially used in the armor model is replaced by the SikaForce^{TM6} 7752-L60 polyurethane adhesive model. The medium mesh size will be used in subsequent simulations.

Table 9: Mode I and II critical energy release rates calculated for interlayer thicknesses of 0.50 mm to 1.50 mm.

Interlayer thickness (mm)	0.50	0.75	1.00	1.25	1.50
G_{IC} (N/m)	1872	2195	2360	2444	2487
G_{IIC} (N/m)	3530	4617	5410	5989	6411

3. Results and discussion

This section explores the effect of: (1) adhesive thicknesses, (2) defects in the adhesive layer, and (3) strain rate dependency in the model on the overall simulated ceramic/metal armor performance. Specifically, the armor performance is evaluated using a comparison of the velocity-history plot, depth of penetration (DOP) of the projectile, and damage patterns of the ceramic plate.

3.1 Effect of adhesive thickness

In this sub-section, the effects of different adhesive thicknesses are explored. Thicknesses varied from 0.50 mm to 1.50 mm with increments of 0.25 mm and are selected based on common thicknesses used in armor applications [3, 4, 5, 6, 7, 41]. To perform these simulations, the dependency of modes 1 and 2 critical energy release rates on the adhesive thicknesses is considered before their implementation in the model following [9]. Using Equation A.1 for mode I loading and Equation A.2 for mode II loading, the new critical energy release rates are evaluated based on the adhesive thickness. The values for γ_I and γ_{II} are first evaluated assuming values for $\tau_I = 2690 \pm 700$ 1/m and $\tau_{II} = 1260 \pm 270$ 1/m and these are taken from Marzi et al. [9] for the SikaForce^{TM6} 498 epoxy adhesive. Using Equations A.1 and A.2 for the 1 mm adhesive thickness case, the $\gamma_I = 2530 \pm 400$ N/m and $\gamma_{II} = 38030 \pm 2840$ N/m values for the SikaForce^{TM6} 7752-L60 polyurethane adhesive are then calculated. The G_{IC} and G_{IIC} values for all thicknesses are then calculated using Equations A.1 and A.2, and the results for these critical energy release rates are summarized in Table 9. The updated thickness-dependent values for G_{IC} and G_{IIC} are implemented in the CZM for the different adhesive thicknesses.

The velocity-time history curves of the rear center node of the projectile for the various adhesive layer thicknesses are presented in Fig. 7. The rear center node of the projectile is chosen to collect the velocity-time history curves to align with the other studies [6, 23]. Fig. 7 shows that the projectile takes longer to reach a complete stop with increasing adhesive thickness, suggesting a relatively inferior armor performance for single impact. While seemingly small, the differences of a few microseconds have been shown to be sufficient for influencing the ability of armor to defeat projectiles [47], including through erosion [46].

Next, the depth of penetration (DOP) is plotted against time for the different adhesive thicknesses in Fig. 8a. As before, the nodes at the deepest location of the hole left by the impactor are used to calculate the DOP for each thickness. The deviations of the DOP curves from using the various adhesive thicknesses begin to become more prominent at approximately 0.02 ms. This is the time it takes for the projectile to fully penetrate the ceramic layer and to start to penetrate the adhesive layer and metal backing. The DOP into the metal backing layer at the end of the simulation is plotted against adhesive thickness as shown in Fig. 8b. Here, the DOP increases with increasing adhesive layer

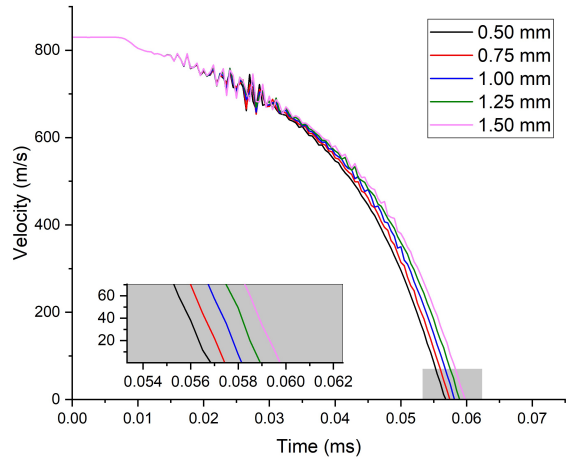

(a)

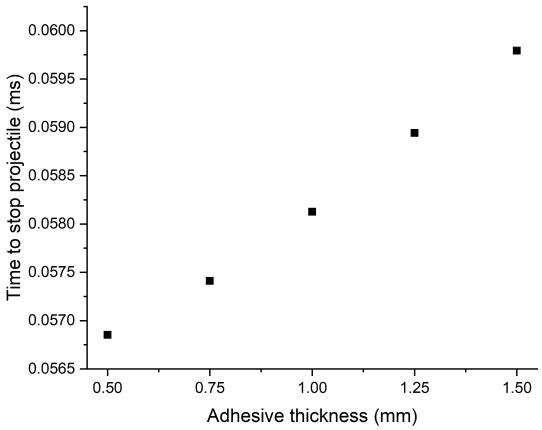

(b)

Figure 7: (a) Velocity-time history of the rear center node of the projectile and (b) time to stop projectile for adhesive layer thicknesses between 0.50 mm and 1.50 mm.

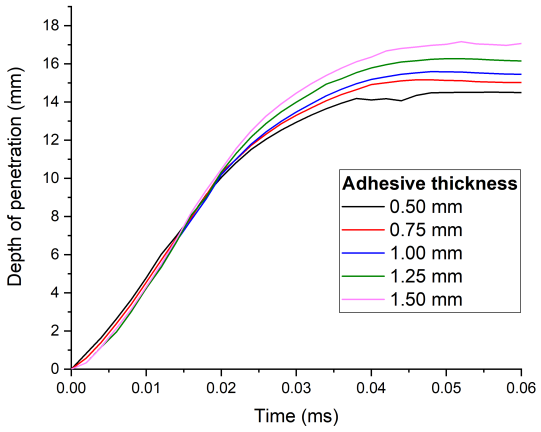

(a)

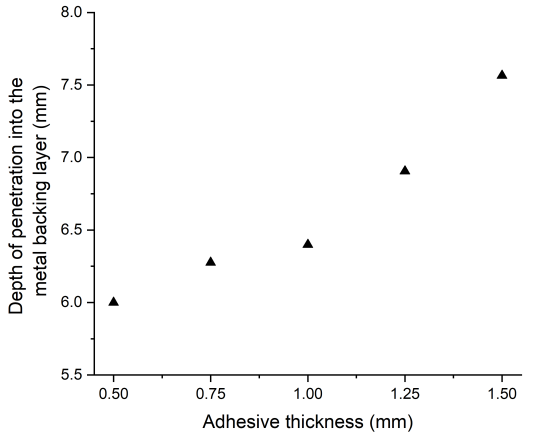

(b)

Figure 8: Depth of projectile penetration (a) plotted against time and (b) into the metal backing layer for adhesive thicknesses between 0.50 mm and 1.50 mm.

thickness and this further suggests that for a single hit, an increase in adhesive thicknesses results in a decrease in armor performance under these conditions. The increasing DOP trend with increasing adhesive thickness is consistent with the study by Shen et al. [5].

Next, the resulting simulated damage patterns of the ceramic tiles for different adhesive thicknesses are presented in Fig. 9 where both the isometric and the cross-sectional views of the ceramic layers are shown. The damage pattern is not symmetric since an asymmetric projectile mesh is used for the simulation, with non-symmetric meshes being used elsewhere in the literature [48, 49, 50, 51]. The overall damage area to the tiles decreases with increasing adhesive thickness. These damage areas weaken the top ceramic tile, thus a decrease in the multi-hit capability of the entire armor system would be expected if the damage was greater. In the literature, it has been shown that the structural integrity of the entire composite system can be weakened from small incremental damage states [18]. From this, the multi-hit capability is, therefore, expected to increase when increasing the adhesive thickness due to reduced fragmentation of the ceramic tiles around the point of impact. These trends with thickness and multi-hit capability are consistent with the ones presented by Shen et al. [5]. In summary, for

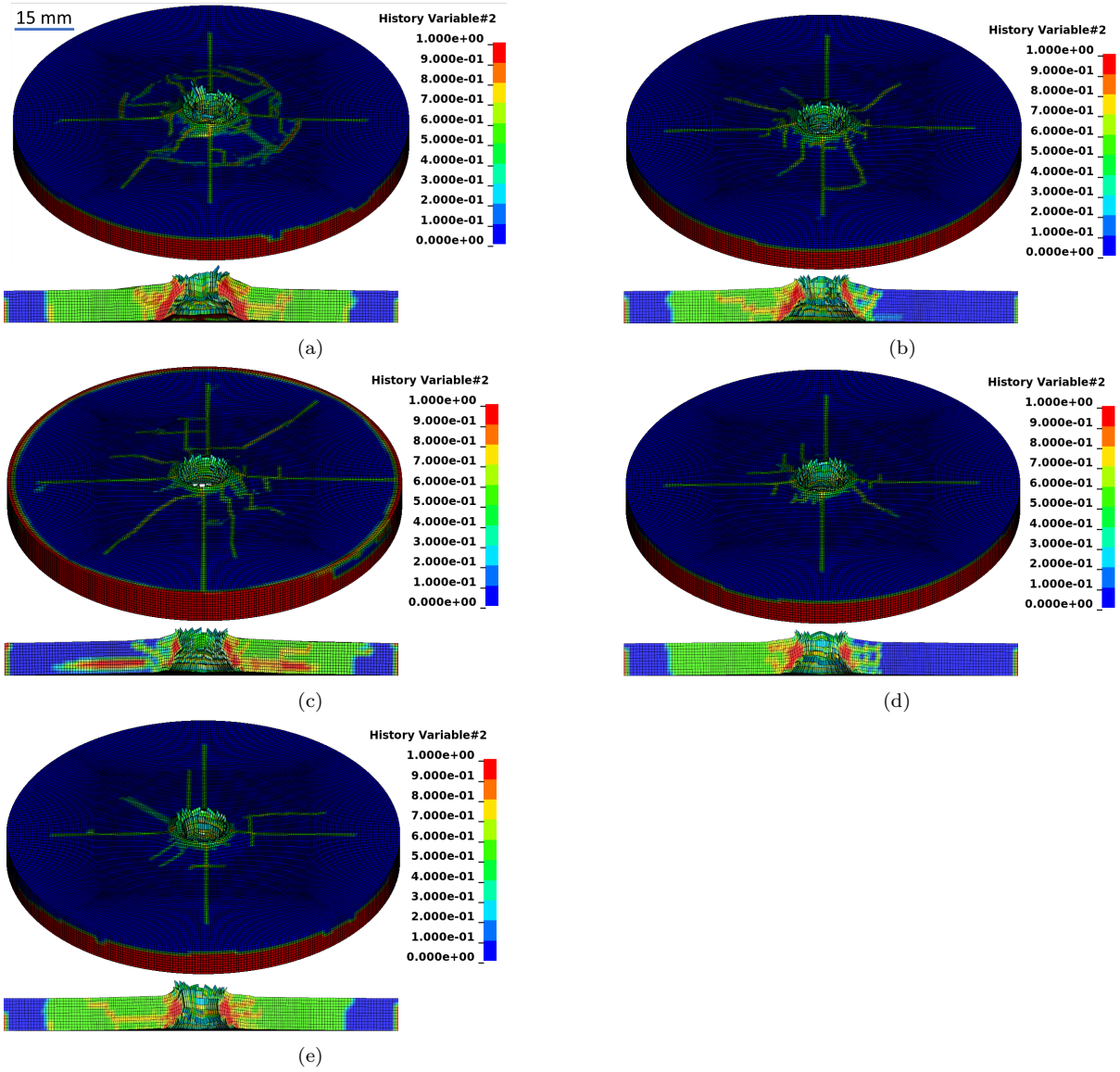

Figure 9: Damage patterns on the alumina ceramic tile for adhesive thicknesses of: (a) 0.50 mm, (b) 0.75 mm, (c) 1.00 mm, (d) 1.25 mm, and (e) 1.50 mm. A cross-sectional view of the ceramic tile is provided below the isometric view for each of the thicknesses.

the conditions simulated (single impact on ceramic/metal armor model), the optimum SikaForce^{TM6} 7752-L60 polyurethane adhesive thickness was found to be 0.5 mm. However, another optimization study must be performed to determine the optimum thickness for multi-impact conditions.

3.2 The role of defects on simulated armor performance

In this sub-section, the effect of introducing gaps or trapped air bubbles in the adhesive layer is explored using simulated voids within the layer. In real-world design, air bubbles can get trapped in the adherend due to the surface roughness during manufacturing, and can induce cracks leading to early or premature failure of an adhesive bond [52]. The gaps within the adhesive layer in these simulations represent structural defects that include inconsistencies in manufacturing and not material defects. In this current study, a MATLAB program is developed to randomly remove elements (specifically 0.5%, 1.5%, 2.5%, 3.75%, 5%, 6.25%, and 7.5% of air bubbles to total surface area ratios) from

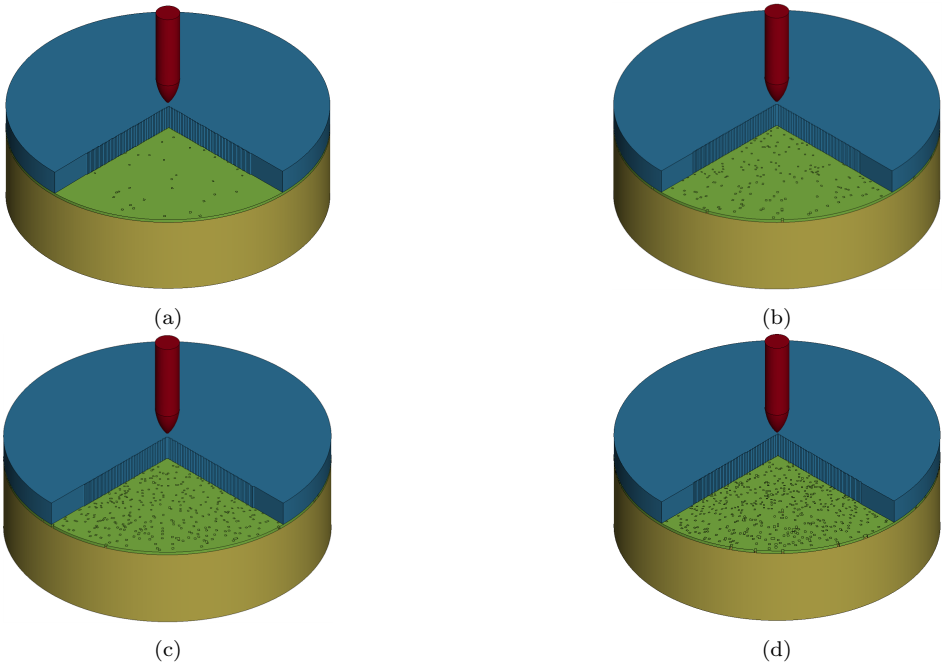

Figure 10: Air bubbles within the adhesive layer represented by deleted cohesive zone elements with gap ratios of: (a) 0.5%, (b) 2.5%, (c) 5%, and (d) 7.5%.

the interlayer, where these gaps are used to represent trapped air bubbles derived from manufacturing. In the code, element positions of the adhesive layer were extracted from the LS-DYNA keyword file, then random elements were deleted through a percentage input in the code. The new element positions were then imported back into the LS-DYNA keyword file. It is assumed that a quality control check is in place during manufacturing when bonding the ceramic to the metal backing and that the number of air bubbles to total surface area does not exceed 7.5%. A schematic showing these defects within the adhesive layer is provided in Fig. 10.

The effect of air bubbles on simulated armor performance is explored. For that purpose, the projectile velocity-time history for all the defect percentage ratios is presented in Fig. 11. This data represents five simulations at each porosity level. The low defect porosities (0% to 2.5%) results in similar times to stop the projectile, but the higher percentage of defects results in a greater time to stop the projectile (> 0.14 microseconds). Again, it is very important to consider the small differences in microseconds for armor applications [46, 47]. The DOP of the projectile for the different defect percentage ratios is plotted in Fig. 12 where each point represents the average of five simulations taken as different realizations of random assignment of defect locations. The error bars in Fig. 12 represent one standard deviation of the uncertainty under these considerations. As before, nodes at the deepest location of the impact crater are taken to calculate the depth of penetration under a given condition. From this figure, the percentage difference between the maximum and minimum DOP values is 0.9%. As seen in both Figs. 11 and 12, a small amount of defects can significantly affect armor performance. Results at low porosities of 0% to 2.5% defect percentage ratios in Fig. 12 suggest that there could be transitional behaviors of DOP for low defect porosities. The DOP and the time taken to stop the projectile at intermediate to high porosities of 2.5% to 7.5% defect percentage ratios are found to be higher than at low porosities. Therefore, the armor systems with the lower porosities within the adhesive layer result in lower DOP values, thereby

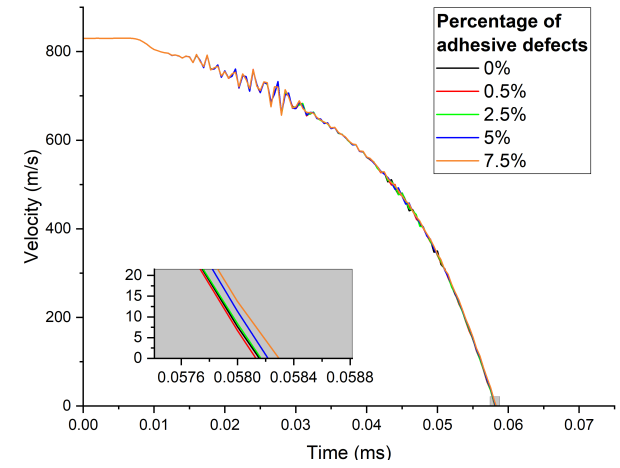

(a)

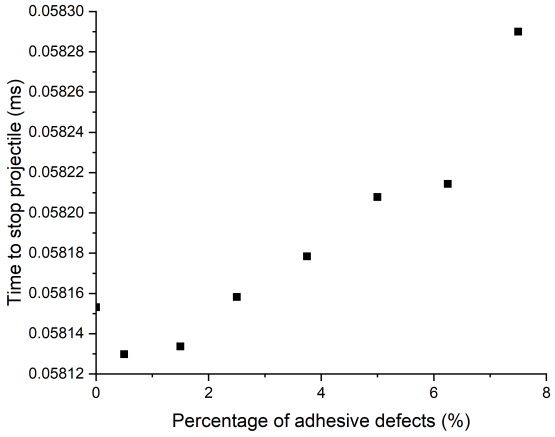

(b)

Figure 11: (a) Velocity-time history of the rear center node of the projectile (1.5%, 3.75%, and 6.25% porosities omitted for clarity) and (b) time to stop projectile for interlayer defect percentage ratios of 0% to 7.5%.

potentially increasing the performance.

3.3 A strain rate-dependent cohesive zone model

Finally, the effects of introducing strain rate-dependent parameters on armor performance are explored. In the literature, similar rate-dependent trends have been reported for epoxy and polyurethane under high compressive loading rates [53] and so strain rate parameters for the 3M^{TM} Scotch-Weld^{TM} AF 163-2OST structural epoxy adhesive are implemented for the proposed SikaForce^{TM6} 7752-L60 polyurethane adhesive cohesive zone model. The strain rate parameters for the epoxy adhesive are obtained from the study by Lißner et al. [54]. The parameters used for the strain rate-dependent cohesive zone model are summarized in Table 10.

To explore the effect of including strain rate dependency in the model on the response of the armor system, a comparison between the velocity-time responses measured at the rear center node for both cases (with and without strain rate dependency) is performed for three projectile velocities (630 m/s, 830 m/s, and 1030 m/s) and is shown in Fig. 13. In the velocity range studied, the results show that strain rate effects do not significantly

Table 10: Trilinear cohesive zone model parameters used to define the SikaForce^{TM6} 7752-L60 polyurethane adhesive in LS-DYNA [26, 28, 29]. Strain rate dependency is considered by including rate-dependent terms of 3M^{TM} Scotch-Weld^{TM} AF 163-2OST structural epoxy adhesive [54].

Model Parameters	Value	Units
Density (ρ) [28]	1.60×10^{3}	kg/m^3
Young's modulus (E) [26]	4.93×10^{8}	Pa
Shear modulus (G) [26]	1.88×10^{8}	Pa
Lower bound of yield strength (T_0) [54]	-3.24×10^{6}	Pa
Upper bound of yield strength (T_1) [54]	-1.80×10^{6}	Pa
Equivalent strain rate term of yield stress ($\dot{\varepsilon}_T$) [54]	0.1	-
Lower bound of shear strength (S_0) [54]	-5.16×10^{6}	Pa
Upper bound of shear strength (S_1) [54]	-1.60×10^{6}	Pa
Equivalent strain rate term of shear stress ($\dot{\varepsilon}_S$) [54]	0.1	-
Lower bound of mode I critical energy release rate (G_{I0}) [54]	-2.36×10^{3}	N/m
Upper bound of mode I critical energy release rate ($G_{I\infty}$) [54]	2.00×10^{3}	N/m
Equivalent strain rate term of mode I critical energy release rate ($\dot{\varepsilon}_{GI}$) [54]	0.1	-
Lower bound of mode II critical energy release rate (G_{II0}) [54]	-5.41×10^{3}	N/m
Upper bound of mode II critical energy release rate ($G_{II\infty}$) [54]	6.5×10^{3}	N/m
Equivalent strain rate term of mode II critical energy release rate ($\dot{\varepsilon}_{GII}$) [54]	0.1	-
Mode I plastic to total area ratio (f_{G1}) [29]	0.13	-
Mode II plastic to total area ratio (f_{G2}) [29]	0.9	-

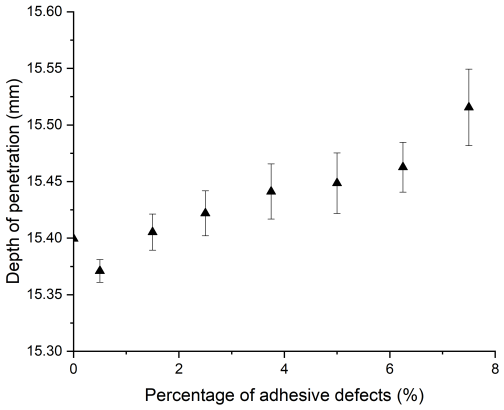

Figure 12: Depth of projectile penetration for interlayer defect percentage ratios of 0% to 7.5%.

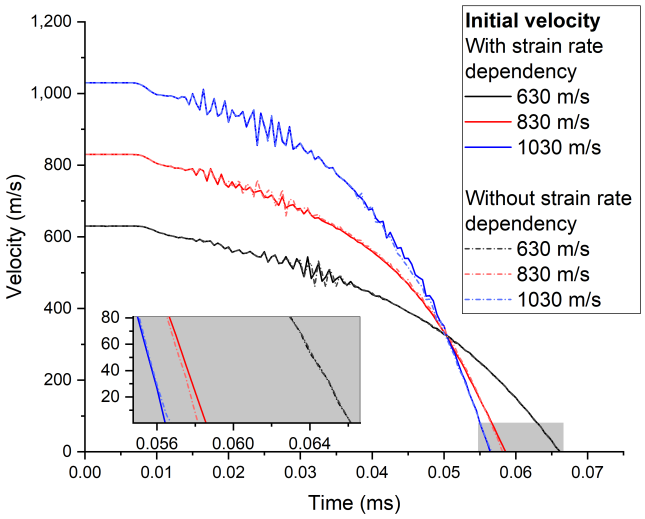

Figure 13: Velocity-time history of the rear center node of the projectile for initial projectile velocities of 630 m/s, 830 m/s, and 1030 m/s with and without the strain rate-dependent model implemented for the adhesive layer constitutive model.

affect the velocity-time profile, only a maximum of 0.8% difference between the two curves for the 830 m/s case. The strain rate effects do not affect the results significantly since the stopping power of the adhesive is minimal. The mechanical response of the adhesive is, however, important for damage induced by high velocity impact since it is related to the bonding and failure of elements. Next, the DOP results obtained for these projectile velocities for both the model with and without strain rate-dependent terms are presented in Table 12. As expected, the DOP increases when increasing the impact velocity for both cases. When including strain rate dependency, there is a negligible DOP increase where at the highest velocity the difference is 0.87 mm.

One significant difference between the two models is the damage area of the adhesive under the impact zone. Schematics of these damage zones for both the model with and without strain rate-dependent terms are presented in Fig. 14 for the 830 m/s case. Similar trends are seen with the other initial velocities, so only the 830 m/s case is presented here. The area of the damage zone (or deleted elements) for the different velocity cases with and without considering strain rate is calculated and presented in Table 11. The 830 m/s case

results in the greatest damage area for both the strain rate and non-strain rate-dependent adhesive models. More importantly, the inclusion of strain rate-dependent terms in the model results in a much larger debonding area for all velocities. This suggests that a decrease in the multi-hit capability of the multilayered structure would be predicted if strain rate dependency was considered due to the larger debonding area of the ceramic layer from the metal backing layer.

Table 11: Adhesive damage area after impact for initial projectile velocities of 630 m/s, 830 m/s, and 1030 m/s with and without the strain rate terms implemented in the adhesive layer constitutive model.

Initial velocity (m/s)	Damage area (mm^2)	
	With strain rate terms	Without strain rate terms
630	870	252
830	2047	421
1030	1690	386

Table 12: Depth of penetration results for initial projectile velocities of 630 m/s, 830 m/s, and 1030 m/s with and without the strain rate terms implemented in the adhesive layer constitutive model.

Initial velocity (m/s)	Depth of penetration (mm)	
	With strain rate terms	Without strain rate terms
630	13.39	13.45
830	14.05	15.57
1030	19.81	20.68

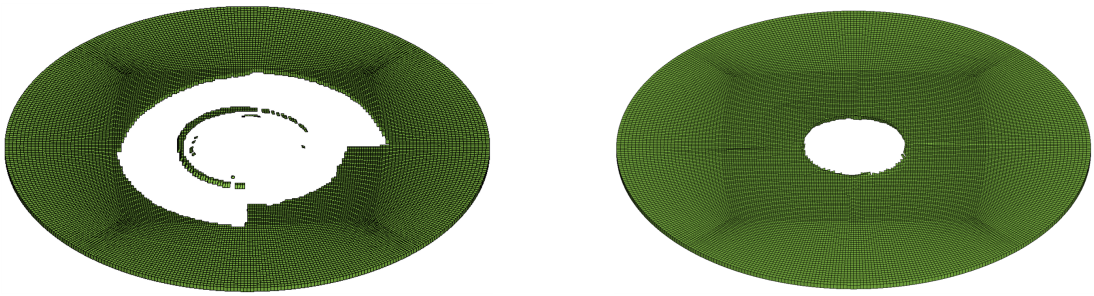

(a) (b)

Figure 14: The damage region of the adhesive (a) with and (b) without implementing the strain rate-dependent terms into the cohesive zone model for the projectile travelling at an initial velocity of 830 m/s.

4. Conclusions

For the first time in the literature, a trilinear cohesive zone model is developed and validated for the SikaForce^{TM6} 7752-L60 polyurethane adhesive to model all phases of its dynamic failure, including elasticity, plasticity, and damage initiation. The model is validated using force-displacement curves of double cantilever beam and end-notched flexure tests published by Faneco et al. [26]. A system-scale armor model consisting of a ceramic tile bonded to an aluminum backing is validated using numerical data such as the velocity-time history and depth of penetration of the projectile. The validated cohesive zone adhesive model for the SikaForce^{TM6} 7752-L60 polyurethane is then implemented into the validated system-scale armor model. This work presents new approaches to analyze and explore the armor model by: (1) investigating the effects of using different interlayer thicknesses and considering the dependency of critical energy release rates to material thickness, (2) introducing adhesive layer defects (manufacturing defects resulting from trapped air bubbles) through a developed MATLAB script to delete random cohesive elements, and (3) incorporating strain rate terms into the adhesive cohesive zone model. Thicker adhesive layers are found to increase the time taken for the projectile to stop and also increase the depth of penetration, thus decreasing simulated armor performance. An increase in the adhesive thickness, however, reduces the damage to the ceramic tile of the layered structure through a subsequent reduction in the damage area of the impact zone. An increase in the percentage of air bubbles in the adhesive layer led to an increasing trend in the depth of penetration and longer times to stop the bullet. Thus, this increase in air bubbles within the adhesive layer would lead to lower ballistic performance in these systems. Introducing the strain rate-dependent terms in the model led to a significant increase of the adhesive debonding/damage region under the impact zone and a decrease in the depth of penetration for all the projectile velocities. Overall, this study opens to: (1) improve upon existing adhesive models to better describe their dynamic behavior under high-velocity impact loadings, and (2) guide the design of armor systems to improve their performance.

Acknowledgments

This work is supported by Defence Research and Development Canada (DRDC), General Dynamics Land Systems–Canada, and NP Aerospace through NSERC Alliance project ALLRP 560447-2020. The views and conclusions contained in this document are those of the authors and should not be interpreted as representing the official policies, either expressed or implied, of General Dynamics, NP Aerospace, DRDC or the Government of Canada. The Government of Canada is authorized to reproduce and distribute reprints for Government purposes notwithstanding any copyright notation herein. This research was enabled in part by support provided by Compute Ontario (www.computeontario.ca/) and Compute Canada (www.computecanada.ca) via the Graham cluster.

Appendix A. Numerical methods

Appendix A.1 Cohesive zone model

To develop a dynamic failure model of adhesives, this study used the CZM approach. The cohesive elements represent the region of expected crack growth in the model [55].

These cohesive elements follow the traction separation law (TSL), which is an approximation to the Griffith's theory of crack growth [56]. CZM has an advantage over traditional finite element methods because it offers a better strength and fracture prediction through choosing the best TSL shape for the material [57]. The traction separation law defines cohesive shear and tension stresses with their respective displacements. With a defined TSL, the cohesive zone can predict the initiation and direction of crack growth [58]. This is possible as the calculation involves combining fracture mechanics with stress-based criteria [11].

A trilinear cohesive mixed-mode elasto-plastic rate material model (`*MAT_COHESIVE_MIXED_MODE_ELASTOPLASTIC_RATE`) available in the LS-DYNA software is used in this study to simulate the dynamic failure behaviour of adhesively bonded joints. The model follows the trilinear (or trapezoidal) TSL as shown in Fig. A.15. The model considers the effects of plasticity and strain rate dependency, and assumes plastic failure during separation [20]. In Fig. A.15, the area under the TSL represents the critical energy release rate of the material, G_C (N/m). The plastic region is the constant stress horizontal line which spans up to damage initiation. The area under the horizontal line is denoted by G_P (N/m). The initial linear portion of the curve assumes the adhesive behaves linear-elastically until the plastic region. Damage is initiated once the plastic region ends, and the adhesive fails when the energy dissipated during crack propagation equals G_C. Furthermore, the mode I and mode II critical energy release rates, G_{IC} (N/m) and G_{IIC} (N/m), are dependent on the adhesive thickness [9]. The relationship between the critical energy release rates and adhesive thickness, t_A (m), is expressed as [9]:

$$G_{IC} = \gamma_I(1 - e^{-\tau_I t_A}) \tag{A.1}$$

$$G_{IIC} = \gamma_{II}(1 - e^{-\tau_{II} t_A}) \tag{A.2}$$

where γ_I (J/m^2), γ_{II} (J/m^2), τ_I (1/m), and τ_{II} (1/m) are constants determined experimentally. The trilinear TSL is chosen over the bilinear TSL since it has the ability to model plasticity and it is a readily available material model in LS-DYNA [20].

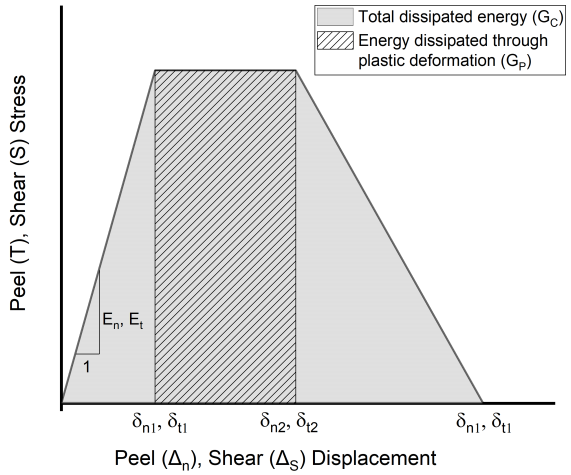

Figure A.15: Trilinear traction separation law used in the cohesive mixed-mode elastoplastic rate material model in LS-DYNA [22].

The separations in the peel, Δ_n (m), and the shear, Δ_t (m), modes are given by [20]:

$$\Delta_n = \langle u_n \rangle \text{ where } \begin{cases} u_n, & \text{if } u_n > 0 \\ 0, & \text{else} \end{cases} \tag{A.3}$$

$$\Delta_t = \sqrt{u_{t1}^2 + u_{t2}^2} \tag{A.4}$$

where u_n (m), u_{t1} (m), and u_{t2} (m) are mode I, II, and III separations, respectively. Mixed-mode separation, Δ_m (m), is defined as [20]:

$$\Delta_m = \sqrt{u_n^2 + u_t^2} \tag{A.5}$$

where u_t (m) is the separation in the shear direction.

The initial stiffnesses of the normal, E_n (Pa), and tangential, E_t (Pa), directions are given by [20]:

$$E_n = E/t_{elem} \text{ and } E_t = G/t_{elem} \tag{A.6}$$

where E (Pa) is the Young's modulus, G (Pa) is the shear modulus, and t_{elem} (m) is the user defined element thickness. For loading modes I and II, the shape of the TSL is defined by the ratios $f_{G1} = G_{IP}/G_{IC}$ and $f_{G2} = G_{IIP}/G_{IIC}$, where G_{iP} (N/m) and G_{iC} (N/m) are the areas under the plastic region and entire curve for $i = 1, 2$ for loading modes I and II, respectively [20]. The equivalent strain rate, $\dot{\varepsilon}_{eq}$ (1/s), is calculated by [20]:

$$\dot{\varepsilon}_{eq} = \frac{\sqrt{\dot{u}_n^2 + \dot{u}_{t_1}^2 + \dot{u}_{t_2}^2}}{t_{elem}} \tag{A.7}$$

where $\dot{u}_n$ (m/s), $\dot{u}_{t_1}$ (m/s), and $\dot{u}_{t_2}$ (m/s) are the velocities in the peel and the two tangential directions, respectively. Tensile, T (Pa), and shear, S (Pa), stresses are calculated as functions of the equivalent strain rates by a linear logarithm function (Equation A.8), and constant values (rate independent) (Equation A.9) [20]:

$$\begin{aligned} T(\dot{\varepsilon}_{eq}) &= T_0 + T_1 \left(\ln \tfrac{\dot{\varepsilon}_{eq}}{\dot{\varepsilon}_T} \right), \text{ if } T_0 < 0, T_1 < 0 \\ S(\dot{\varepsilon}_{eq}) &= S_0 + S_1 \left(\ln \tfrac{\dot{\varepsilon}_{eq}}{\dot{\varepsilon}_S} \right), \text{ if } S_0 < 0, S_1 < 0 \end{aligned} \tag{A.8}$$

$$\begin{aligned} T(\dot{\varepsilon}_{eq}) &= T_0, \text{ if } T_0 > 0 \\ S(\dot{\varepsilon}_{eq}) &= S_0, \text{ if } S_0 > 0 \end{aligned} \tag{A.9}$$

where S_0 (Pa) and T_0 (Pa) are the lower bounds of shear and yield strengths, and S_1 (Pa) and T_1 (Pa) are the upper bounds of shear and yield strengths. Similarly, fracture energies in mode I loading, G_{IC} (Pa/m) and mode II loading, G_{IIC} (Pa/m) are calculated as being rate-dependent (Equation A.10) and rate independent (Equation A.11) [20]:

$$\begin{aligned} G_{IC}(\dot{\varepsilon}_{eq}) &= G_{I0} + (G_{I\infty} - G_{I0}) \exp \tfrac{\dot{\varepsilon}_{GI}}{\dot{\varepsilon}_{eq}}, \text{ if } G_{I0} < 0 \\ G_{IIC}(\dot{\varepsilon}_{eq}) &= G_{I0} + (G_{II\infty} - G_{II0}) \exp \tfrac{\dot{\varepsilon}_{GII}}{\dot{\varepsilon}_{eq}}, \text{ if } G_{II0} < 0 \end{aligned} \tag{A.10}$$

$$\begin{aligned} G_{IC}(\dot{\varepsilon}_{eq}) &= G_{I0}, \text{ if } G_{I0} > 0 \\ G_{IIC}(\dot{\varepsilon}_{eq}) &= G_{II0}, \text{ if } G_{II0} > 0 \end{aligned} \tag{A.11}$$

where G_{I0} (Pa/m) and G_{II0} (Pa/m) are the lower bounds of modes I and II critical energy release rates, $G_{I\infty}$ (Pa/m) and $G_{II\infty}$ (Pa/m) are the upper bounds of modes I and II

critical energy release rates, and $\dot{\varepsilon}_{GI}$ (1/s) and $\dot{\varepsilon}_{GII}$ (1/s) are the equivalent strain rate at yield initiation to describe the rate dependency of G_{IC} and G_{IIC}, respectively. Next, the mixed-mode behavior is evaluated.

The mixed-mode yield initiation, δ_{m1} (m), damage initiation, δ_{m2} (m), and final displacements, δ_{mf} (m), are formulated using a quadratic initiation criterion given by [20]:

$$\delta_{m1} = \delta_{n1}\delta_{t1}\sqrt{\frac{1+\beta^2}{\delta_{t1}^2 + (\beta\delta_{n1})^2}} \tag{A.12}$$

$$\delta_{m2} = \delta_{n2}\delta_{t2}\sqrt{\frac{1+\beta^2}{\delta_{t2}^2 + (\beta\delta_{n2})^2}} \tag{A.13}$$

$$\delta_{mf} = \frac{\delta_{m1}(\delta_{m1}-\delta_{m2})E_n G_{IIC}\cos\gamma^2 + G_{IC}(2G_{IIC} + \delta_{m1}(\delta_{m1}-\delta_{m2})E_t\sin\gamma^2)}{\delta_{m1}(E_n G_{IIC}\cos\gamma^2 + E_t G_{IC}\sin\gamma^2)} \tag{A.14}$$

where $\delta_{n1} = \frac{T}{E_n}$ (m) and $\delta_{t1} = \frac{S}{E_t}$ (m) are the single-mode yield initiation displacements, $\beta = \frac{\delta_{t1}}{\delta_{n1}}$ is the mixed-mode ratio, $\delta_{n2} = \delta_{n1} + \frac{f_{G1}G_{IC}}{T}$ (m), $\delta_{t1} = \delta_{t1} + \frac{f_{G2}G_{IIC}}{S}$ (m) are the single-mode damage initiation displacements, and parameter $\gamma = \arccos\frac{u_n}{\Delta_m}$. Plastic separation in the peel direction, $u_{n,P}$ (m), and the shear elastic separation, $\delta_{t,y}$ (m), are given by [20]:

$$u_{n,P} = \max\left(u_{n,P,\Delta t-1}, u_n - \delta_{m1}\sin\gamma, 0\right) \tag{A.15}$$

$$\delta_{t,y} = \sqrt{(u_{t1} - u_{t1,P,t_i-1})^2 + (u_{t2} - u_{t2,P,t_i-1})^2} \tag{A.16}$$

The plastic shear separations in mode I, $u_{t1,P}$ (m), and mode II, $u_{t1,P}$ (m), become: [20]:

$$u_{t1,P} = u_{t1,P,t_{i-1}} + u_{t1} - u_{t1,t_{i-1}} \tag{A.17}$$

$$u_{t2,P} = u_{t2,P,t_{i-1}} + u_{t2} - u_{t2,t_{i-1}} \tag{A.18}$$

when $\delta_{t,y} > \delta_{m1}\sin\gamma$ and where t_{i-1} (s) is the previous timestep value.

The damage parameter, D_{CZM}, is defined as [20]:

$$D_{\mathrm{CZM}} = \max\frac{\Delta_m - \delta_{m2}}{\delta_{mf} - \delta_{m2}}, D_{\mathrm{CZM},\Delta t-1}, 0 \tag{A.19}$$

and is initiated once $\Delta_m > \delta_{m2}$. The element fully fails ($D_{\mathrm{CZM}} = 1$) when $\Delta_m > \delta_{mf}$. Once the damage parameter is solved, the peel, σ_{ti} (Pa), and shear stresses, σ_n, are calculated using [20]:

$$\sigma_{t1} = E_t(1 - D_{\mathrm{CZM}})(u_{t1} - u_{t1,P}) \tag{A.20}$$

$$\sigma_{t2} = E_t(1 - D_{\mathrm{CZM}})(u_{t2} - u_{t1,2}) \tag{A.21}$$

$$\sigma_n = \begin{cases} E_n(1 - D_{\mathrm{CZM}})(u_n - u_{n,P}), & \text{if } u_n - u_{n,P} > 0 \\ E_n(u_n - u_{n,P}), & \text{if } u_n - u_{n,P} \leq 0 \end{cases} \tag{A.22}$$

The parameters for this material model are later validated using experimental results from Faneco et al. [26] for the SikaForce$^{\mathrm{TM6}}$ 7752-L60 polyurethane adhesive. Once validated, this cohesive zone material model is used to simulate the dynamic failure behavior of the polyurethane adhesive bonding a ceramic plate to a metal backing during high-velocity impact conditions.

Appendix A.2 Johnson-Holmquist II material model

The Johnson-Holmquist II (JH2) material model (`*MAT_JOHNSON_HOLMQUIST_CERAMICS`) is used to model the 99.5% purity alumina ceramic tile of the layered structure [23]. The JH2 model is a popular damage model to represent the behavior of brittle materials subjected to large strains, strain rates, and pressures [37]. Many studies have used the JH2 material model to simulate ceramic tiles undergoing ballistic impact [7, 11, 23, 40, 43].

In the model, the normalized equivalent stress, σ^*_{JH2}, is defined as [59]:

$$\sigma^*_{\text{JH2}} = \sigma^*_{i,\text{JH2}} - D_{\text{JH2}}(\sigma^*_{i,\text{JH2}} - \sigma^*_{f,\text{JH2}}) \tag{A.23}$$

where D_{JH2} is a damage parameter bounded within $0 \leq D_{\text{JH2}} \leq 1$, $\sigma^*_{i,\text{JH2}}$ is the intact undamaged behavior when $D_{\text{JH2}} = 0$, and $\sigma^*_{f,\text{JH2}}$ is the damaged behavior when $D_{\text{JH2}} = 1$. The equivalent stress, and damaged and undamaged behavior are normalized by the Hugoniot Elastic Limit (HEL) to be made dimensionless through [59]:

$$\sigma^*_{\text{JH2}} = \frac{\sigma}{\sigma_{\text{HEL}}} \tag{A.24}$$

The intact undamaged and damaged behavior are defined as [59]:

$$\sigma^*_{i,\text{JH2}} = a_{\text{JH2}}(p^* + t^*)^{n_{\text{JH2}}}(1 + c_{\text{JH2}} \ln \dot{\varepsilon}^*) \tag{A.25}$$

$$\sigma^*_{f,\text{JH2}} = b_{\text{JH2}}(p^*)^{m_{\text{JH2}}}(1 + c_{\text{JH2}} \ln \dot{\varepsilon}^*) \tag{A.26}$$

where a_{JH2}, b_{JH2}, c_{JH2} (1/s), m_{JH2}, and n_{JH2} are material constants, $\dot{\varepsilon}^*$ is the normalized plastic strain rate, and t^* and p^* are normalized maximum tensile hydrostatic pressure and normalized pressure, respectively. The superscripts are used since similar terms are presented later to define Johnson-Cook material model equations. The pressure term, p_{JH2} (Pa), and maximum tensile fracture strength, t (Pa), is normalized by the HEL through [59]:

$$p^* = \frac{p_{\text{JH2}}}{p_{\text{HEL}}} \tag{A.27}$$

$$t^* = \frac{t}{p_{\text{HEL}}} \tag{A.28}$$

The damage parameter, D_{JH2}, is accumulated through [59]:

$$D_{\text{JH2}} = \sum \frac{\Delta\varepsilon^p}{\varepsilon^p_f} \tag{A.29}$$

where ε^p and ε^p_f are the incremental plastic deformation and rate independent plastic strain to fracture, respectively. The plastic strain to fracture, ε^p_f, is given by [59]:

$$\varepsilon^p_f = d_1(p^* + t^*)^{d_2} \tag{A.30}$$

where d_1 and d_2 are material constants. Pressure is defined using an equation of state [59]:

$$p_{\text{JH2}} = k_1\mu + k_2\mu^2 + k_3\mu^3 + \Delta p \tag{A.31}$$

where k_1 (Pa), k_2 (Pa), and k_3 (Pa) are experimentally determined constants, and μ_{JH2} and Δp are the excess compression and pressure increment, respectively. Δp is only added

once damage begins to accumulate ($D_{\text{JH2}} > 0$). The excess compression, μ, and pressure increment, $\Delta p_{t+\Delta t}$ (Pa), are given by [59]:

$$\mu_{\text{JH2}} = \frac{\rho_{\text{JH2}}}{\rho_{0,\text{JH2}}} - 1 \tag{A.32}$$

$$\Delta p_{t+\Delta t} = -k_1\mu_t + \sqrt{(k_1\mu_t + \Delta p_t)^2 + 2\beta_{\text{JH2}}k_1\Delta U} \tag{A.33}$$

where $\rho_{0,\text{JH2}}$ (kg/m^3) and ρ_{JH2} (kg/m^3) are the initial and final densities, respectively, ΔU (J) is the incremental energy loss between successive damage states, and β_{JH2} is the fraction of elastic energy converted to potential energy. The subscript t (s) is the previous time step and $t + \Delta t$ (s) is the current time step. In this study, the JH2 material model is used to simulate impact into a 99.5% alumina ceramic plate. The parameters for this model are validated using numerical results of a system-scale armor model taken from the literature [6, 23] and the parameters are provided in Table 4.

Appendix A.3 Johnson-Cook material model

The Johnson-Cook (JC) material model (`*MAT_JOHNSON_COOK`) is implemented for both the 7.62 mm surrogate projectile and the aluminum Al5083 H116 metal backing [23]. The JC model is a well-studied phenomenological model describing the behavior of metals undergoing large deformation, high strain rates, and high temperatures [36, 41]. Thus, this model has been widely used to simulate the response of metals undergoing high-velocity impact [11, 23, 43, 41, 60].

In the JC model, the flow stress, σ_y (Pa), is defined as [36]:

$$\sigma_y = \left(a_{\text{JC}} + b_{\text{JC}}\overline{\varepsilon}^{p^{*n_{\text{JC}}}}\right)\left(1 + c_{\text{JC}}\ln\dot{\varepsilon}^*\right)\left(1 - T^{*m_{\text{JC}}}\right) \tag{A.34}$$

where a_{JC} (Pa), b_{JC} (Pa), c_{JC}, m_{JC}, and n_{JC} are material constants, $\overline{\varepsilon}^{p^*}$ is the effective plastic strain, and $\dot{\varepsilon}^*$ and T^* are the effective plastic strain and normalized temperature. These are defined as [36]:

$$\dot{\varepsilon}^* = \frac{\overline{\varepsilon}^{p^*}}{\dot{\varepsilon}_0} \tag{A.35}$$

$$T^* = \frac{T - T_{\text{room}}}{T_{\text{melt}} - T_{\text{room}}} \tag{A.36}$$

where $\dot{\varepsilon}_0 = 1$ (1/s), and T (K), T_{room} (K), and T_{melt} (K) are the current temperature, room temperature, and melting temperature, respectively. The strain at fracture, ε^f, is given by [61]:

$$\varepsilon^f = (D_1 + D_2\exp D_3\sigma^*)(1 + D_4\ln\varepsilon^*)(1 + D_5T^*) \tag{A.37}$$

where D_1 to D_5 are material constants and σ^* is the effective stress defined as [61]:

$$\sigma^* = \frac{p_{\text{JC}}}{\sigma_{\text{eff}}} \tag{A.38}$$

where p_{JC} (Pa) and σ_{eff} (Pa) are the pressure and effective stress terms, respectively. The damage, D_{JC}, is accumulated through [61]:

$$D_{\text{JC}} = \sum \frac{\overline{\varepsilon}^{p^*}}{\varepsilon^f} \tag{A.39}$$

where fracture occurs when $D_{\mathrm{JC}} = 1$.

The equation of state relating pressure to volume is given by the linear relationship expressed as:

$$P = C_1 \mu_{\mathrm{JC}} \tag{A.40}$$

where C_1 (Pa) is the bulk modulus and μ_{JC} is the excess compression term given by:

$$\mu_{\mathrm{JC}} = \frac{\rho_{\mathrm{JC}}}{\rho_{0,\mathrm{JC}}} - 1 \tag{A.41}$$

where ρ_{JC} (kg/m^3) is the initial density and $\rho_{0,\mathrm{JC}}$ (kg/m^3) is the final density. This material model is also used to simulate the high-velocity impact behavior of a steel 4340 projectile and for an aluminum Al5083 H116 metal backing. The parameters for this model are validated using numerical results of a system-scale armor model from the literature [6, 23] and are provided in Table 5.

Appendix A.4 Cowper-Symonds strength model

The epoxy adhesive used for the ceramic/armor validation case is described using the Cowper-Symonds strength model following the simulations performed by Prakash et al. [6] and Rashed et al. [23]. Here, the material is described by the Mie-Gruneisen equation of state (`*EOS_GRUNEISEN`) [23], and the density is defined by using the null material model (`*MAT_NULL`). The Mie-Gruneisen equation of state relates pressure and volume at a given temperature. The pressure term is defined as [62]:

$$p = \frac{\rho_0 C^2 \mu (1 + (1 - \frac{\gamma_0}{2})\mu - \frac{a}{2}\mu^2)}{1 + (S_{\mathrm{MG},1} - 1)\mu - S_{\mathrm{MG},2}\frac{\mu^2}{\mu+1} - S_{\mathrm{MG},3}\frac{\mu^3}{(\mu+1)^2}} + (\gamma_0 + a\mu)E \tag{A.42}$$

$$p = \rho_0 C^2 \mu + (\gamma_0 + a\mu)E \tag{A.43}$$

for compressed and expanded solids, respectively, where γ_0 is the unitless Gruneisen gamma, a is a unitless first order volume correction to γ_0, ρ_0 (kg/m^3) is the material density, E (Pa) is the elastic modulus, C and $S_{\mathrm{MG},1}$ to $S_{\mathrm{MG},3}$ are the intercept and unitless coefficients to the cubic shock-velocity versus particle velocity curve, respectively, and μ is the excess compression term defined in Equation A.41.

Appendix B. Numerical test set up of the double cantilever beam and end-notched flexure tests

A numerical model of the double cantilever beam (DCB) and end-notched flexure (ENF) test setups are created which replicate the experimental work of Faneco et al. [26]. A meshed three-dimensional geometry with element size of 1 mm for the DCB and ENF tests are shown in Fig. B.16. The load is applied 50 mm away from the initial crack region of the adhesive for the DCB test on the top adherend. The hinge is also located 50 mm away from the initial crack region and on the bottom adherend. The hinges for the ENF test are located on the bottom adherend 15 mm inwards from both sides of the test specimen. These hinge placement locations are shown in Fig. B.17 for the DCB and ENF tests and were obtained through correspondence from Faneco et al. [26].

In the simulations, 4-point cohesive elements (termed `ELFORM EQ19` in LS-DYNA) are used for the adhesive layer, and fully integrated hexahedron solid elements (`ELFORM EQ2`) are used for the adherend. An additional contact setting (`*AUTOMATIC_SURFACE_TO_SURFACE`) is needed to define the sliding contact between adherend layers in the ENF test.

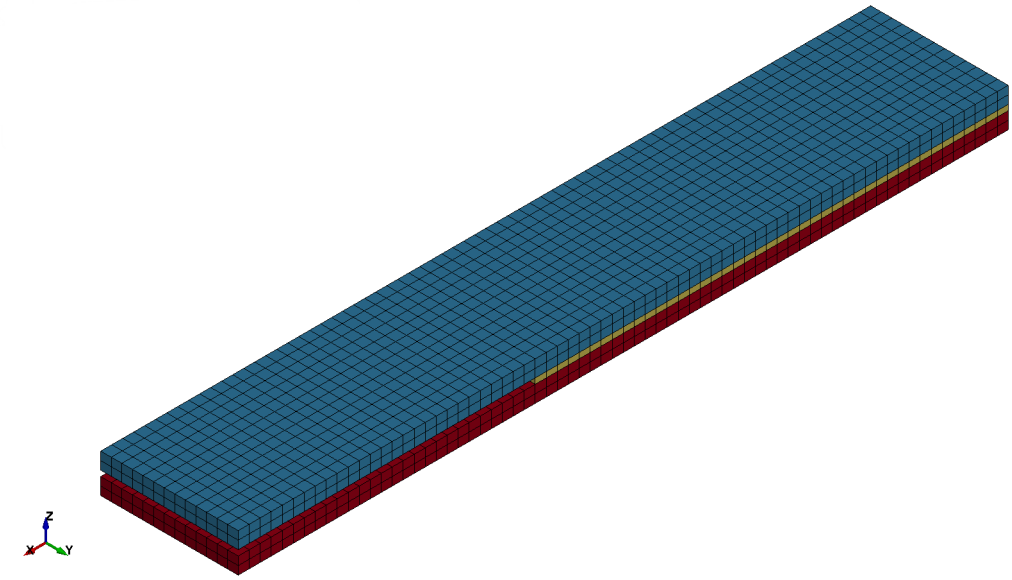

(a)

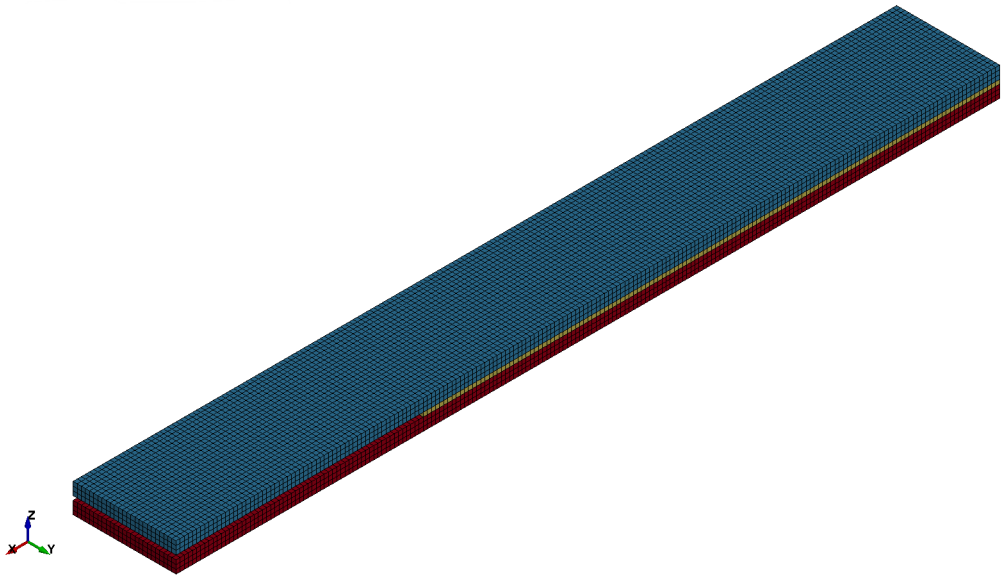

(b)

Figure B.16: Isometric view of the mesh for (a) the double cantilever beam and (b) the end-notched flexure test setups with an element size of 1 mm based on the experimental work performed by Faneco et al. [26].

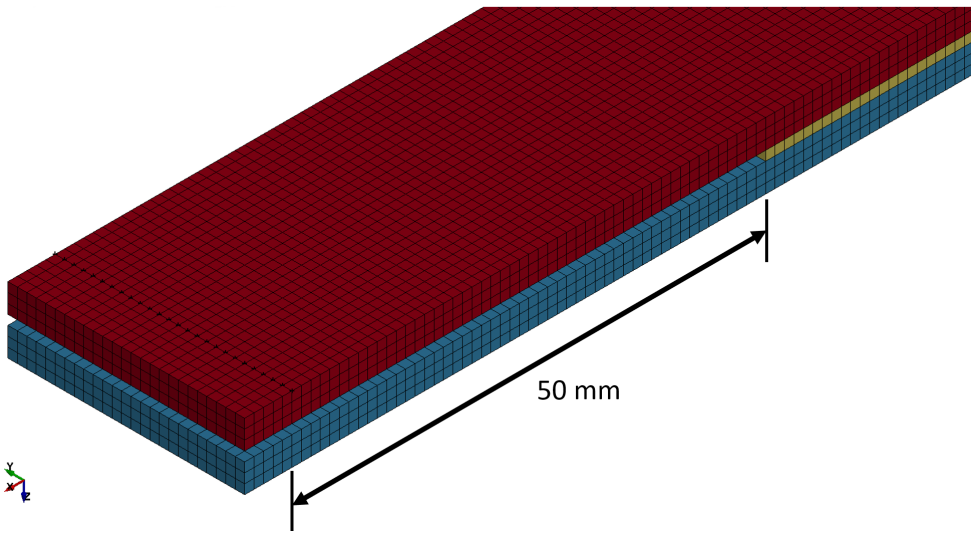

(a)

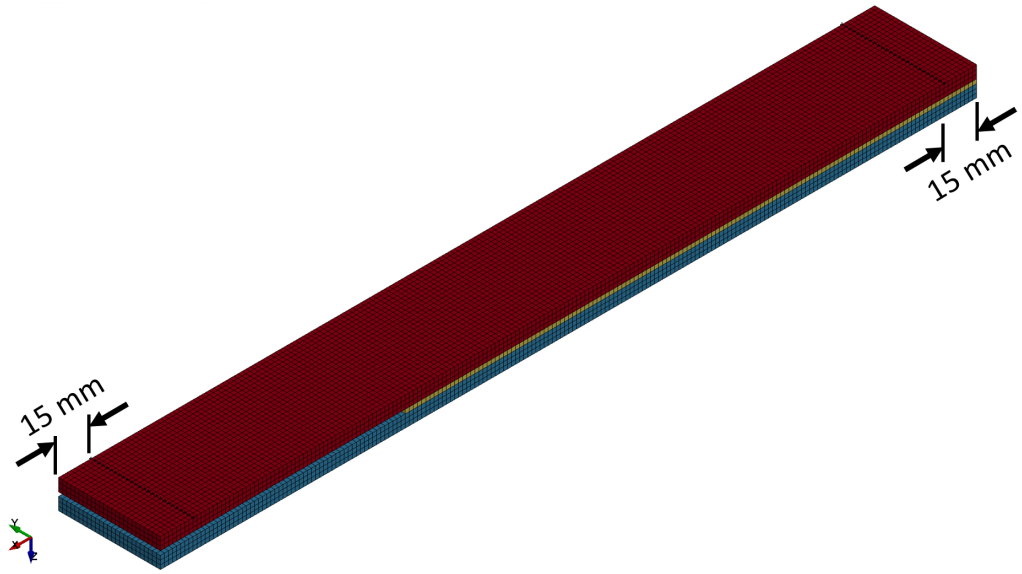

(b)

Figure B.17: Hinge placement locations on (a) the double cantilever beam and (b) the end-notched flexure test setups based on the experimental work performed by Faneco et al. [26].

Appendix C. Element formulation and contact settings for the ceramic/metal armor model

This section discusses element type and the contact settings used for the ceramic/armor model. The element type used for discretization are formulated using the constant stress solid element (`EQ1`). The (`*AUTOMATIC_SURFACE_TO_SURFACE`) is contact is used between the three layers of the ceramic/metal armor model (from Fig. 4) where all default values are used. To simulate the erosion of the projectile and the three layers of the composite structure, an eroding surface to surface contact is applied (`*ERODING_SURFACE_TO_SURFACE`) where: (1) the erosion/interior node option (`EROSOP`) is set as 1 to allow for erosion; (2) the adjacent material treatment for solid element (`IADJ`) parameter is set as 1 to allow for self-erosion (erosion between adjacent elements within a single part); (3) the soft constraint option (`SOFT`) is set to 2 for pinball segment based contact to allow for the model to produce contact forces; and (4) the segment-based contact option (`SBOPT`) is set to the recommended value of 3 when setting `SOFT`= 2. Lastly, a tied contact (`*TIED_SURFACE_TO_SURFACE`) is applied between the layers of the composite structure to simulate the adhesive bonding where all default values are used.

References

[1] M. Grujicic, B. Pandurangan, and B. d'Entremont, "The role of adhesive in the ballistic/structural performance of ceramic/polymer–matrix composite hybrid armor," *Materials Design*, vol. 41, pp. 380–393, 2012.

[2] K. Chatzikypraios, "Advanced technologies for the bonding and de-bonding of armour structures (armourbond)," Nov 2019.

[3] R. Zaera, S. Sánchez-Sáez, J. Pérez-Castellanos, and C. Navarro, "Modelling of the adhesive layer in mixed ceramic/metal armours subjected to impact," *Composites Part A: Applied Science and Manufacturing*, vol. 31, no. 8, pp. 823–833, 2000.

[4] J. Puente, A. Arias, R. Zaera, and C. Navarro, "The effect of the thickness of the adhesive layer on the ballistic limit of ceramic/metal armors. an experimental and numerical study," *International Journal of Impact Engineering*, vol. 32, 12 2005.

[5] Y. Shen, Y. Wang, S. Du, Z. Yang, H. Cheng, and F. Wang, "Effects of the adhesive layer on the multi-hit ballistic performance of ceramic/metal composite armors," *Journal of Materials Research and Technology*, vol. 13, pp. 1496–1508, 2021.

[6] A. Prakash, J. Rajasankar, N. Anandavalli, M. Verma, and N. R. Iyer, "Influence of adhesive thickness on high velocity impact performance of ceramic/metal composite targets," *International Journal of Adhesion and Adhesives*, vol. 41, pp. 186–197, 2013.

[7] K. Arslan and R. Gunes, "Ballistic impact simulation of ceramic/metal armor structures," *Uluslararası Muhendislik Arastirma ve Gelistirme Dergisi*, pp. 12–18, 12 2017.

[8] W. Seifert, E. Strassburger, S. Grefen, and S. Schaare, "Experimental study about the influence of adhesive stiffness to the bonding strengths of adhesives for ceramic/metal targets," *Defence Technology*, vol. 12, no. 2, pp. 188–200, 2016. 2016 International Symposium on Ballistics.

[9] S. Marzi, "An extension of MAT 240 to consider the failure of structural adhesive joints in crash simulations," in *German LS-Dyna Forum, conference proceedings, Bamberg*, 2010.

[10] B. Watson, M. J. Worswick, and D. S. Cronin, "Quantification of mixed mode loading and bond line thickness on adhesive joint strength using novel test specimen geometry," *International Journal of Adhesion and Adhesives*, vol. 102, p. 102682, 2020.

[11] D. Bürger, A. Rocha de Faria, S. F. de Almeida, F. C. de Melo, and M. V. Donadon, "Ballistic impact simulation of an armour-piercing projectile on hybrid ceramic/fiber reinforced composite armours," *International Journal of Impact Engineering*, vol. 43, pp. 63–77, 2012.

[12] G. Akhmet, Y. Yu, P. Hu, W. bin Hou, and X. Han, "Analysis of the performance of adhesively bonded corrugated core sandwich structures using cohesive zone method," *Journal of Sandwich Structures & Materials*, vol. 22, no. 1, pp. 104–124, 2020.

[13] A. Guilpin, G. Franciere, L. Barton, M. Blacklock, and M. Birkett, "A numerical and experimental study of adhesively-bonded polyethylene pipelines," *Polymers*, vol. 11, no. 9, 2019.

[14] M. Gurvich, "Fracture modeling and characterization of elastomeric materials and composites for design applications," *Rubber Chemistry and Technology*, vol. 83, pp. 368–379, 12 2010.

[15] D. Silva, R. Campilho, and U. Carvalho, "Application a direct/cohesive zone method for the evaluation of scarf adhesive joints," *Applied Adhesion Science*, vol. 6, 12 2018.

[16] L. Hamitouche, M. Tarfaoui, and A. Vautrin, "An interface debonding law subject to viscous regularization for avoiding instability: application to the delamination problems," *Engineering Fracture Mechanics*, vol. 75, no. 10, pp. 3084–3100, 2008.

[17] A. Maziz, M. Tarfaoui, S. Rechak, M. Nachtane, and L. Gemi, "Finite element analysis of impact-induced damage in pressurized hybrid composites pipes," *Int. J. Appl. Mech*, vol. 13, p. 2150074, 2021.

[18] A. Maziz, M. Tarfaoui, L. Gemi, S. Rechak, and M. Nachtane, "A progressive damage model for pressurized filament-wound hybrid composite pipe under low-velocity impact," *Composite Structures*, vol. 276, p. 114520, 2021.

[19] I. Goda and J. Girardot, "Numerical modeling and analysis of the ballistic impact response of ceramic/composite targets and the influence of cohesive material parameters," *International Journal of Damage Mechanics*, vol. 30, no. 7, pp. 1079–1122, 2021.

[20] S. Marzi, O. Hesebeck, M. Brede, and F. Kleiner, "A rate-dependent , elasto-plastic cohesive zone mixed-mode model for crash analysis of adhesively bonded joints," 2009.

[21] Z. Jia, G. Yuan, X. Feng, and Y. Zou, "Numerical study on the mechanical behavior of a polyurethane adhesive under high strain rate," *Composites Part B: Engineering*, vol. 158, pp. 131–140, 2019.

[22] Livermore Software Technology Corporation, *LS-DYNA version 11.1*, 2007. https://www.lstc.com/products/ls-dyna.

[23] A. Rashed, M. Yazdani, A. Babaluo, and P. H. Parvin, "Investigation on high-velocity impact performance of multi-layered alumina ceramic armors with polymeric interlayers," *Journal of Composite Materials*, vol. 50, no. 25, pp. 3561–3576, 2016.

[24] J. Lemaitre and R. Desmorat, *Engineering Damage Mechanics: Ductile, Creep, Fatigue and Brittle Failures*, ch. 1, pp. 1–76. Springer Nature, 2005.

[25] *The mathematical Theory of Plasticity*, ch. 6, pp. 137–190. John Wiley Sons, Ltd, 2008.

[26] T. Faneco, R. Campilho, and R. Lopes, "Strength and fracture characterization of a novel polyurethane adhesive for the automotive industry," *Journal of Testing and Evaluation*, vol. 45, pp. 398–407, 03 2017.

[27] S. Cardamone, A. Bernasconi, and M. Giglio, "Characterization of the 3m scotch-weld™ 7260 b/a epoxy adhesive by cohesive damage models and application to a full-scale bonded sub-structure," *The Journal of Adhesion*, vol. 96, pp. 1270–1301, 10 2020.

[28] Sika Industry, *SikaForce-7752 FRW L60*, 6 2013. Version 1, https://deu.sika.com/de/industrie/marine/kleben-und-dichtenimboots-undschiffbau/sandwichpaneele-undmoebelteile/sikaforce-472-frl60.html.

[29] Y. B. Liu, "Application of a rate dependent cohesive zone model to predict impact response in adhesively bonded ultra-high strength steel tubes," Master's thesis, University of Waterloo, 2019.

[30] L. Shengze, F. Jin, Z. Weihua, and X. Meng, "Research of hail impact on aircraft wheel door with lattice hybrid structure," *Journal of Physics: Conference Series*, vol. 744, p. 012102, 09 2016.

[31] Livermore Software Technology Corporation, *LS-DYNA Keyword User's Manual*, 2007. https://www.dynasupport.com/manuals.

[32] C. Desai, S. Basu, and V. Parameswaran, "Determination of traction separation law for interfacial failure in adhesive joints at different loading rates," *The Journal of Adhesion*, vol. 92, p. 150527102921008, 05 2015.

[33] R. Fernandes and R. Campilho, "Testing different cohesive law shapes to predict damage growth in bonded joints loaded in pure tension," *The Journal of Adhesion*, vol. 93, 03 2016.

[34] A. Guilpin, G. Franciere, L. Barton, M. Blacklock, and M. Birkett, "A numerical and experimental study of adhesively-bonded polyethylene pipelines," *Polymers*, vol. 11, no. 9, 2019.

[35] Altair Engineering Incorporation, *HyperWorks*, 2021. https://www.altair.com/hyperworks/.

[36] "A constitutive model and data for metals subjected to large strains, high strain rates and high temperatures," *Proceedings of the Seventh International Symposium on Ballistics*, 1983.

[37] G. R. Johnson and T. J. Holmquist, "An improved computational constitutive model for brittle materials," in *High-pressure Science and technology - 1993*, vol. 309 of *American Institute of Physics Conference Series*, pp. 981–984, 1994.

[38] D. Cronin, K. Bui, C. Kaufmann, G. Mcintosh, and T. Berstad, "Implementation and validation of the Johnson-Holmquist ceramic material model in LS-DYNA," *4th European LS-DYNA Users Conference*, pp. 47–60, 01 2003.

[39] E. Flores-Johnson, L. Shen, I. Guiamatsia, and G. D. Nguyen, "Numerical investigation of the impact behaviour of bioinspired nacre-like aluminium composite plates," *Composites Science and Technology*, vol. 96, pp. 13–22, 2014.

[40] D. Luo, Y. Wang, F. Wang, H. Cheng, B. Zhang, and Y. Zhu, "The influence of metal cover plates on ballistic performance of silicon carbide subjected to large-scale tungsten projectile," *Materials Design*, vol. 191, p. 108659, 2020.

[41] Y. Gao, W. Zhang, P. Xu, X. Cai, and Z. Fan, "Influence of epoxy adhesive layer on impact performance of TiB2-B4C composites armor backed by aluminum plate," *International Journal of Impact Engineering*, vol. 122, pp. 60–72, 2018.

[42] R. Chi, A. Serjouei, I. Sridhar, and G. E. Tan, "Ballistic impact on bi-layer alumina/aluminium armor: A semi-analytical approach," *International Journal of Impact Engineering*, vol. 52, pp. 37–46, 2013.

[43] G. Toussaint and I. Polyzois, "Steel spheres impact on alumina ceramic tiles:experiments and finite element simulations," *International Journal of Applied Ceramic Technology*, vol. 16, 06 2019.

[44] A. Bhattacharjee, A. Bhaduri, R. C. Hurley, and L. Graham-Brady, "Failure Modeling and Sensitivity Analysis of Ceramics Under Impact," *Journal of Applied Mechanics*, vol. 88, 02 2021. 051007.

[45] W. L. Goh, B. Luo, W. Xu, and Y. Jianming, "Simulation study on influence of component thickness on dwell-penetration transition time of long rod projectile impacting ceramic armour module," *Journal of Physics: Conference Series*, vol. 1721, p. 012015, 01 2021.

[46] A. B. Dresch, J. Venturini, S. Arcaro, O. R. Montedo, and C. P. Bergmann, "Ballistic ceramics and analysis of their mechanical properties for armour applications: A review," *Ceramics International*, vol. 47, no. 7, Part A, pp. 8743–8761, 2021.

[47] B. Koch, P. Jannotti, D. Mallick, B. Schuster, T. Sano, and J. Hogan, "Influence of microstructure on the impact failure of alumina," *Materials Science and Engineering: A*, vol. 770, p. 138549, 10 2019.

[48] D. F. Gordon, B. Hafizi, Y. Khine, and S. Douglass, "Ballistics modeling for non-axisymmetric hypervelocity smart bullets," tech. rep., NAVAL RESEARCH LAB WASHINGTON DC BEAM PHYSICS BRANCH, 2014.

[49] G. H. Yoon, J. S. Mo, K. H. Kim, C. H. Yoon, and N. H. Lim, "Investigation of bullet penetration in ballistic gelatin via finite element simulation and experiment," *Journal of Mechanical Science and Technology*, vol. 29, no. 9, pp. 3747–3759, 2015.

[50] A. M. Soydan, B. Tunaboylu, A. G. Elsabagh, A. K. Sarı, and R. Akdeniz, "Simulation and experimental tests of ballistic impact on composite laminate armor," *Advances in materials science and engineering*, vol. 2018, 2018.

[51] G. Mo, Q. Ma, Y. Jin, W. Yan, Z. Li, and Z. Wu, "Delamination process in cross-ply UHMWPE laminates under ballistic penetration," *Defence Technology*, vol. 17, no. 1, pp. 278–286, 2021.

[52] J. M. A. Reina, J. J. N. Prìeto, and C. A. García, "Influence of the surface finish on the shear strength of structural adhesive joints and application criteria in manufacturing processes," *The Journal of Adhesion*, vol. 85, no. 6, pp. 324–340, 2009.

[53] M. Martínez, I. Chocron, J. Rodríguez, V. Sánchez Gálvez, and L. Sastre, "Confined compression of elastic adhesives at high rates of strain," *International Journal of Adhesion and Adhesives*, vol. 18, no. 6, pp. 375–383, 1998.

[54] M. Lißner, E. Alabort, B. Erice, H. Cui, and N. Petrinic, "A rate dependent experimental and numerical analysis of adhesive joints under different loading directions," *The European Physical Journal Special Topics*, vol. 227, pp. 85–97, 09 2018.

[55] P. Beaurepaire and G. Schuëller, "Modeling of the variability of fatigue crack growth using cohesive zone elements," *Engineering Fracture Mechanics*, vol. 78, no. 12, pp. 2399–2413, 2011.

[56] A. Turon, C. Dávila, P. Camanho, and J. Costa, "An engineering solution for mesh size effects in the simulation of delamination using cohesive zone models," *Engineering Fracture Mechanics*, vol. 74, no. 10, pp. 1665–1682, 2007.

[57] R. Campilho, M. Banea, J. Neto, and L. da Silva, "Modelling adhesive joints with cohesive zone models: effect of the cohesive law shape of the adhesive layer," *International Journal of Adhesion and Adhesives*, vol. 44, pp. 48–56, 2013.

[58] S. Song, G. Paulino, and W. Buttlar, "Simulation of crack propagation in asphalt concrete using an intrinsic cohesive zone model," *Journal Of Engineering Mechanics-Asce*, vol. 132, pp. 1215–, 11 2006.

[59] G. A. Gazonas, "Implementation of the Johnson-Holmquist II (JH-2) constitutive model into DYNA3D," tech. rep., Army Research Lab Aberdeen Proving Ground MD Weapons and Materials Research Directorate, 2002.

[60] C. Tian, Q. Sun, X. An, P. Ye, and Y. Dong, "Influences of ceramic constraint on protection performances of ceramic-metal hybrid structures under impact loads," *International Journal of Mechanical Sciences*, vol. 159, pp. 81–90, 2019.

[61] G. R. Johnson and W. H. Cook, "Fracture characteristics of three metals subjected to various strains, strain rates, temperatures and pressures," *Engineering Fracture Mechanics*, vol. 21, no. 1, pp. 31–48, 1985.

[62] Y. Xiao, H. Wu, and X. Ping, "On the simulation of fragmentation during the process of ceramic tile impacted by blunt projectile with sph method in ls-dyna," *Computer Modeling in Engineering Sciences*, vol. 122, pp. 923–954, 01 2020.